Observation of inverse Compton emission from a long γ-ray burst

https://doi.org/10.1038/s41586-019-1754-6

Received: 20 July 2019

Accepted: 18 October 2019

Published online: 20 November 2019

A list of authors and affiliations appears at the end of the paper.

Long-duration γ-ray bursts (GRBs) originate from ultra-relativistic jets launched from the collapsing cores of dying massive stars. They are characterized by an initial phase of bright and highly variable radiation in the kiloelectronvolt-to-megaelectronvolt band, which is probably produced within the jet and lasts from milliseconds to minutes, known as the prompt emission[1,2]. Subsequently, the interaction of the jet with the surrounding medium generates shock waves that are responsible for the afterglow emission, which lasts from days to months and occurs over a broad energy range from the radio to the gigaelectronvolt bands[1–6]. The afterglow emission is generally well explained as synchrotron radiation emitted by electrons accelerated by the external shock[7–9]. Recently, intense long-lasting emission between 0.2 and 1 teraelectronvolts was observed from GRB 190114C[10,11]. Here we report multi-frequency observations of GRB 190114C, and study the evolution in time of the GRB emission across 17 orders of magnitude in energy, from 5×10^{-6} to 10^{12} electronvolts. We find that the broadband spectral energy distribution is double-peaked, with the teraelectronvolt emission constituting a distinct spectral component with power comparable to the synchrotron component. This component is associated with the afterglow and is satisfactorily explained by inverse Compton up-scattering of synchrotron photons by high-energy electrons. We find that the conditions required to account for the observed teraelectronvolt component are typical for GRBs, supporting the possibility that inverse Compton emission is commonly produced in GRBs.

On 14 January 2019, following an alert from the Neil Gehrels Swift Observatory (hereafter Swift) and the Fermi satellite, the Major Atmospheric Gamma Imaging Cherenkov (MAGIC) telescopes observed and detected radiation up to at least 1 TeV from GRB 190114C. Before the MAGIC detection, GRB emission had only been reported at much lower energies, below 100 GeV, first by CGRO-EGRET and more recently by AGILE-GRID and Fermi-LAT (see ref. [12] for a recent review).

Detection of teraelectronvolt radiation opens a new window in the electromagnetic spectrum for the study of GRBs[10]. Its announcement[13] triggered an extensive campaign of follow-up observations. Owing to the relatively low redshift of $z = 0.4245 \pm 0.0005$ (Methods) of the GRB (corresponding to a luminosity distance of about 2.3 Gpc), a comprehensive set of multi-wavelength data could be collected. We present observations gathered from instruments onboard six satellites and 15 ground telescopes (radio, submillimetre, near-infrared (NIR), optical, ultraviolet (UV), and very-high-energy γ-rays; see Methods) for the first ten days after the burst. The frequency range covered by these observations spans more than 17 orders of magnitude, from 1 to about 2×10^{17} GHz, the most extensive so far for a GRB. The light curves of GRB 190114C at different frequencies are shown in Fig. 1.

The prompt emission of GRB 190114C was simultaneously observed by several space missions covering the spectral range from 8 keV to about 100 GeV (Methods). The prompt light curve shows a complex temporal structure with several emission peaks (Methods, Extended Data Fig. 1), with a total duration of about 25 s (see dashed line in Fig. 1) and total radiated energy of $E_{\gamma,\mathrm{iso}} = (2.5 \pm 0.1)\times10^{53}$ erg (isotropic equivalent; 1 erg = 10^{-7} J) in the energy range 1–10^4 keV (ref. [14]). During the time of inter-burst quiescence, at $t \approx 5$–15 s, and after the end of the last prompt pulse, at $t \gtrsim 25$ s, the flux decays smoothly, following a power law of $F \propto t^{\alpha}$ as a function of time t with $\alpha_{10\text{–}1{,}000\mathrm{keV}} = -1.10 \pm 0.01$ (ref. [14]). The temporal and spectral characteristics of this smoothly varying component support an interpretation in terms of afterglow synchrotron radiation, making this one of the few clear cases of afterglow emission detected in the band 10–10^4 keV during the prompt-emission phase. The onset of the afterglow component is then estimated to occur around $t \approx 5$–10 s (refs. [14,15]), implying an initial bulk Lorentz factor between 300 and 700 (Methods).

After about one minute from the start of the prompt emission, two additional high-energy telescopes began observations: MAGIC and Swift-XRT. The XRT (1–10 keV; blue data points in Fig. 1) and MAGIC (0.3–1 TeV; green data points in Fig. 1) light curves decay with time as a power law with decay indices of $\alpha_{\mathrm{X}} \approx -1.36 \pm 0.02$ and $\alpha_{\mathrm{TeV}} \approx -1.51 \pm 0.04$, respectively. The 0.3–1-TeV light curve shown in Fig. 1 was obtained after correcting for attenuation by the extragalactic background light (EBL)[10]. The teraelectronvolt-band emission is observable until about 40 min—much longer than the nominal duration of the prompt-emission phase. The NIR–optical light curves (square symbols) show a more complex behaviour. Initially, a fast decay is seen, where the emission is probably dominated by the reverse-shock component[16]. This is followed by a shallower decay, and subsequently a faster decay at $t \gtrsim 10^5$ s. The latter may indicate that the characteristic synchrotron frequency ν_{m} crosses the optical band (Extended Data Fig. 6), which is not atypical,

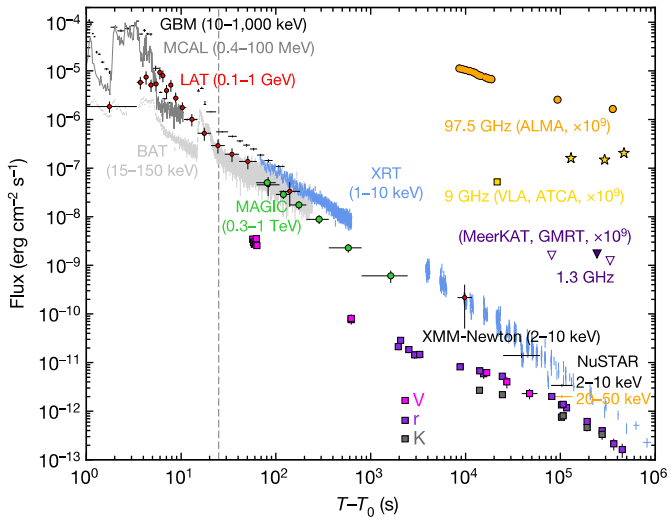

Fig. 1 | Multi-wavelength light curves of GRB 190114C. Energy flux at different wavelengths, from radio to γ-rays, versus time after the BAT trigger, at T_0 = 20:57:03.19 universal time (UT) on 14 January 2019. The light curve for the energy range 0.3–1 TeV (green circles) is compared with light curves at lower frequencies. Those for VLA (yellow square), ATCA (yellow stars), ALMA (orange circles), GMRT (purple filled triangle) and MeerKAT (purple open triangles) have been multiplied by 10^9 for clarity. The vertical dashed line marks approximately the end of the prompt-emission phase, identified as the end of the last flaring episode. For the data points, vertical bars show the 1σ errors on the flux, and horizontal bars represent the duration of the observation. The fluxes in the V, r and K filters (pink, purple and grey filled squares, respectively) have been corrected for extinction in the host and in our Galaxy; the contribution from the host galaxy has been subtracted.

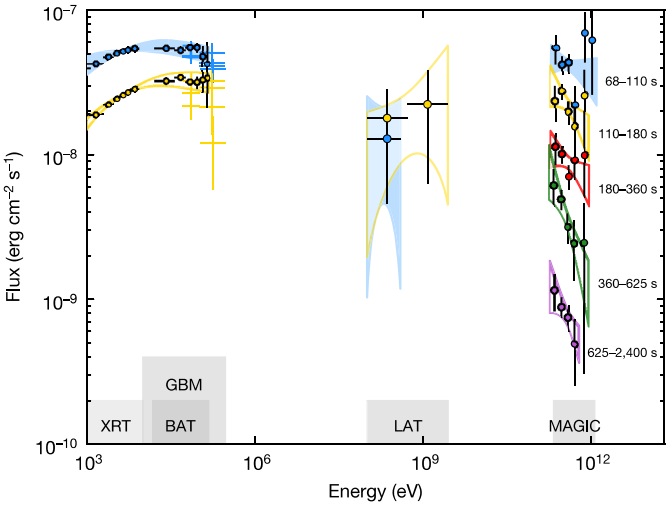

Fig. 2 | Multi-band spectra in the time interval 68–2,400 s. Five time intervals are considered: 68–110 s (blue), 110–180 s (yellow), 180–360 s (red), 360–625 s (green) and 625–2,400 s (purple). MAGIC data points have been corrected for attenuation caused by the EBL. Data from other instruments (Swift-XRT, Swift-BAT, Fermi-GBM and Fermi-LAT) are shown for the first two time intervals. For each time interval, LAT contour regions are shown, limiting the energy to the range in which photons are detected. MAGIC and LAT contour regions are drawn from the 1σ error of their best-fit power-law functions. For Swift data, the regions show the 90% confidence contours for the joint fit for XRT and BAT, obtained by fitting a smoothly broken power law to the data. Filled regions are used for the first time interval (68–110 s).

but usually occurs at earlier times. The relatively late time at which the break appears in GRB 190114C would then imply a very large value of ν_m, placing it in the X-ray band at about 10^2 s. The millimetre light curves (orange symbols) also show an initial fast decay in which the emission is dominated by the reverse shock, followed by emission at late times with nearly constant flux (Extended Data Fig. 3).

The spectral energy distributions (SEDs) of the radiation detected by MAGIC are shown in Fig. 2, where the whole duration of the emission detected by MAGIC is divided into five time intervals. For the first two time intervals, observations in the gigaelectronvolt and X-ray bands are also available. During the first time interval (68–110 s; blue data points and blue confidence regions), Swift-XRT, Swift-BAT and Fermi-GBM data show that the afterglow synchrotron component peaks in the X-ray band. At higher energies, up to 1 GeV, the SED is a decreasing function of energy, as supported by the Fermi-LAT flux between 0.1 and 0.4 GeV (Methods). On the other hand, at even higher energies, the MAGIC flux above 0.2 TeV implies a spectral hardening. This evidence is independent of the EBL model adopted to correct for the attenuation (Methods). This demonstrates that the newly discovered teraelectronvolt radiation is not a simple extension of the known afterglow synchrotron emission, but a separate spectral component.

The extended duration and the smooth, power-law temporal decay of the radiation detected by MAGIC (see green data points in Fig. 1) suggest an intimate connection between the teraelectronvolt emission and the broadband afterglow emission. The most natural candidate is synchrotron self-Compton (SSC) radiation in the external forward shock: the same population of relativistic electrons responsible for the afterglow synchrotron emission Compton up-scatters the synchrotron photons, leading to a second spectral component that peaks at higher energies. Teraelectronvolt afterglow emission can also be produced by hadronic processes, such as synchrotron radiation by protons accelerated to ultrahigh energies in the forward shock[17–19]. However, owing to their typically low radiation efficiency[6], reproducing the luminous teraelectronvolt emission observed here by such processes would imply unrealistically large power of accelerated protons[10]. Teraelectronvolt photons can also be produced via the SSC mechanism in internal shock synchrotron models of the prompt emission. However, numerical modelling (Methods) shows that prompt SSC radiation can account at most for a limited fraction (≲20%) of the observed teraelectronvolt flux, and only at early times ($t \lesssim 100$ s). Henceforth, we focus on the SSC process in the afterglow.

SSC emission has been predicted for GRB afterglows[9,12,18,20–27]. However, its quantitative significance has been uncertain because the SSC luminosity and spectral properties depend strongly on the poorly constrained physical conditions in the emission region (for example, the magnetic field strength). The detection of the teraelectronvolt component in GRB 190114C and the availability of multi-band observations offer the opportunity to investigate the relevant physics at a deeper level. SSC radiation may have been already detected in very bright GRBs, such as GRB 130427A, in which photons with energies of 10–100 GeV are challenging to explain by synchrotron processes, suggesting a different origin[28–30].

We model the full dataset (from the radio band to teraelectronvolt energies, for the first week after the explosion) as synchrotron plus SSC radiation, within the framework of the theory of afterglow emission from external forward shocks. The detailed modelling of the broadband emission and its evolution with time is presented in Methods. We discuss here the implications for the emission at $t < 2{,}400$ s and energies above >1 keV.

The soft spectra in the 0.2–1-TeV energy range (photon index $\Gamma_{\rm TeV} < -2$; see Extended Data Table 1) constrain the peak of the SSC component to below this energy range. The relatively small ratio between the spectral peak energies of the SSC ($E_{\rm p}^{\rm SSC} \lesssim 200$ GeV) and synchrotron ($E_{\rm p}^{\rm syn} \approx 10$ keV) components implies a relatively low value for the electron Lorentz factor ($\gamma \approx 2 \times 10^3$). This value is hard to reconcile with the

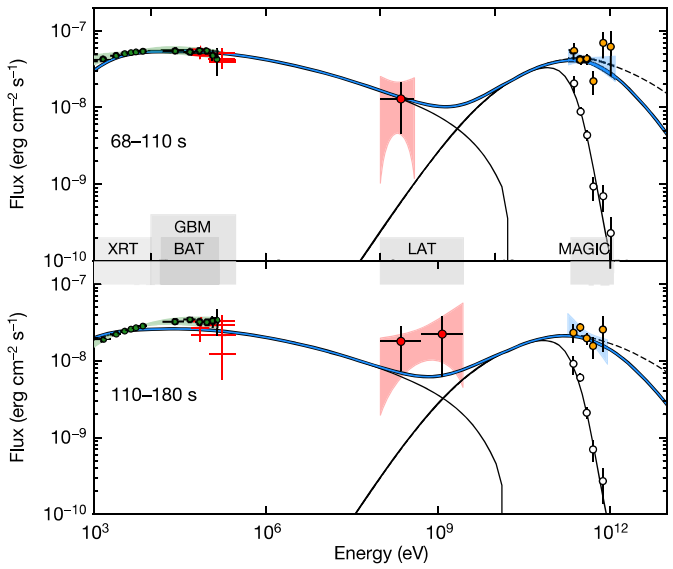

Fig. 3 | Modelling of the broadband spectra in the time intervals 68–110 s and 110–180 s. Thick blue curve, modelling of the multi-band data in the synchrotron and SSC afterglow scenario. Thin solid lines, synchrotron and SSC (observed spectrum) components. Dashed lines, SSC when internal γ–γ opacity is neglected. The adopted parameters are: $s = 0$, $\varepsilon_e = 0.07$, $\varepsilon_B = 8 \times 10^{-5}$, $p = 2.6$, $n_0 = 0.5$ and $E_k = 8 \times 10^{53}$ erg; see Methods. Empty circles show the observed MAGIC spectrum, that is, uncorrected for attenuation caused by the EBL. Contour regions and data points are as in Fig. 2.

observation of the synchrotron peak at energies higher than kiloelectronvolt. To explain the soft spectrum detected by MAGIC, it is necessary to invoke scattering in the Klein–Nishina regime for the electrons radiating at the spectral peak, as well as internal γ–γ absorption[31]. Although both of these effects tend to become less important with time, the spectral index in the 0.2–1-TeV band remains constant in time (or possibly evolves to softer values; Extended Data Table 1). This implies that the SSC peak energy moves to lower energies and crosses the MAGIC energy band. The energy at which attenuation by internal pair production becomes important indicates that the bulk Lorentz factor is about 140–160 at 100 s.

An example of the theoretical modelling in this scenario is shown in Fig. 3 (blue solid curve; see Methods for details). The dashed line shows the SSC spectrum when internal absorption is neglected. The thin solid line shows the model spectrum including EBL attenuation, in comparison to the MAGIC observations (empty circles).

We find that acceptable models of the broadband SED can be obtained if the conditions at the source are the following. The initial kinetic energy of the blast wave is $E_k \gtrsim 3 \times 10^{53}$ erg (isotropic-equivalent). The electrons swept up from the external medium are efficiently injected into the acceleration process and carry a fraction $\varepsilon_e \approx 0.05$–$0.15$ of the energy dissipated at the shock. The acceleration mechanism produces an electron population characterized by a non-thermal energy distribution, described by a power law with index $p \approx 2.4$–2.6, an injection Lorentz factor of $\gamma_m = (0.8\text{–}2) \times 10^4$ and a maximum Lorentz factor of $\gamma_{max} \approx 10^8$ (at about 100 s). The magnetic field behind the shock conveys a fraction $\varepsilon_B \approx (0.05\text{–}1) \times 10^{-3}$ of the dissipated energy. At $t \approx 100$ s, corresponding to a distance from the central engine of $R \approx (8\text{–}20) \times 10^{16}$ cm, the density of the external medium is $n \approx 0.5$–$5\ \mathrm{cm}^{-3}$ and the magnetic field strength is $B \approx 0.5$–5 G. The latter implies that the magnetic field was efficiently amplified from values of a few microgauss, which are typical of the unshocked ambient medium, owing to plasma instabilities or other mechanisms[6]. Not surprisingly, we find that $\varepsilon_e \gg \varepsilon_B$, which is a necessary condition for the efficient production of SSC radiation[18,20].

The blast-wave energy inferred from the modelling is comparable to the amount of energy released in the form of radiation during the prompt phase. The prompt-emission mechanism must then have dissipated and radiated no more than half of the initial jet energy, leaving the rest for the afterglow phase. The modelling of the multi-band data also allows us to infer how the total energy is shared between the synchrotron and SSC components. The resultant powers of the two components are comparable. We estimate that the energy in the synchrotron and SSC component are about 1.5×10^{52} erg and around 6.0×10^{51} erg, respectively, in the time interval 68–110 s, and about 1.3×10^{52} erg and around 5.4×10^{51} erg, respectively, in the time interval 110–180 s. Thus, previous studies of GRBs may have been missing a substantial fraction of the energy emitted during the afterglow phase that is essential to its understanding.

Finally, we note that the values of the afterglow parameters inferred from the modelling fall within the range of values typically inferred from broadband (radio to gigaelectronvolt) studies of GRB afterglow emission. This points to the possibility that SSC emission in GRBs may be a relatively common process that does not require special conditions to be produced, and its power is similar to that of synchrotron radiation.

The SSC component may then be detectable at teraelectronvolt energies in other relatively energetic GRBs, as long as the redshift is low enough to avoid severe attenuation by the EBL. This also provides support to earlier indications for SSC emission at gigaelectronvolt energies[28–30].

1. Mészáros, P. Theories of gamma-ray bursts. *Annu. Rev. Astron. Astrophys.* **40**, 137–169 (2002).
2. Piran, T. The physics of gamma-ray bursts. *Rev. Mod. Phys.* **76**, 1143–1210 (2005).
3. van Paradijs, J., Kouveliotou, C. & Wijers, R. A. M. J. Gamma-ray burst afterglows. *Annu. Rev. Astron. Astrophys.* **38**, 379–425 (2000).
4. Gehrels, N., Ramirez-Ruiz, E. & Fox, D. B. Gamma-ray bursts in the Swift era. *Annu. Rev. Astron. Astrophys.* **47**, 567–617 (2009).
5. Gehrels, N. & Mészáros, P. Gamma-ray bursts. *Science* **337**, 932–936 (2012).
6. Kumar, P. & Zhang, B. The physics of gamma-ray bursts & relativistic jets. *Phys. Rep.* **561**, 1–109 (2015).
7. Sari, R., Piran, T. & Narayan, R. Spectra and light curves of gamma-ray burst afterglows. *Astrophys. J. Lett.* **497**, 17–20 (1998).
8. Granot, J. & Sari, R. The shape of spectral breaks in gamma-ray burst afterglows. *Astrophys. J.* **568**, 820–829 (2002).
9. Mészáros, P. & Rees, M. J. Delayed GeV emission from cosmological gamma-ray bursts – impact of a relativistic wind on external matter. *Mon. Not. R. Astron. Soc.* **269**, L41–L43 (1994).
10. MAGIC Collaboration. Teraelectronvolt emission from the γ-ray burst GRB 190114C. *Nature* https://doi.org/10.1038/s41586-019-1750-x (2019).
11. Mirzoyan, R. et al. MAGIC detects the GRB 190114C in the TeV energy domain. *GCN Circulars* 23701 https//gcn.gsfc.nasa.gov/gcn3/23701.gcn3 (2019).
12. Nava, L. High-energy emission from gamma-ray bursts. *Int. J. Mod. Phys. D* **27**, 1842003 (2018).
13. Mirzoyan, R. et al. MAGIC detects the GRB 190114C. *The Astronomer's Telegram* 12390 http://www.astronomerstelegram.org/?read=12390 (2019).
14. Ajello, M. et al. Fermi and Swift observations of GRB 190114C: tracing the evolution of high-energy emission from prompt to afterglow. Preprint at https://arxiv.org/abs/1909.10605 (2019).
15. Ravasio, M. E. et al. GRB 190114C: from prompt to afterglow? *Astron. Astrophys.* **626**, A12 (2019).
16. Laskar, T. et al. ALMA detection of a linearly polarized reverse shock in GRB 190114C. *Astrophys. J. Lett.* **878**, 26 (2019).
17. Vietri, M. GeV photons from ultrahigh energy cosmic rays accelerated in gamma ray bursts. *Phys. Rev. Lett.* **78**, 4328–4331 (1997).
18. Zhang, B. & Mészáros, P. High-energy spectral components in gamma-ray burst afterglows. *Astrophys. J.* **559**, 110–122 (2001).
19. Razzaque, S. A leptonic–hadronic model for the afterglow of gamma-ray burst 090510. *Astrophys. J. Lett.* **724**, 109–112 (2010).
20. Sari, R. & Esin, A. A. On the synchrotron self-Compton emission from relativistic shocks and its implications for gamma-ray burst afterglows. *Astrophys. J.* **548**, 787–799 (2001).

21. Mészáros, P., Razzaque, S. & Zhang, B. GeV–TeV emission from γ-ray bursts. *New Astron. Rev.* **48**, 445–451 (2004).
22. Lemoine, M. The synchrotron self-Compton spectrum of relativistic blast waves at large *Y. Mon. Not. R. Astron. Soc.* **453**, 3772–3784 (2015).
23. Fan, Y.-Z. & Piran, T. High-energy γ-ray emission from gamma-ray bursts – before GLAST. *Front. Phys. China* **3**, 306–330 (2008).
24. Galli, A. & Piro, L. Prospects for detection of very high-energy emission from GRB in the context of the external shock model. *Astron. Astrophys.* **489**, 1073–1077 (2008).
25. Nakar, E., Ando, S. & Sari, R. Klein–Nishina effects on optically thin synchrotron and synchrotron self-Compton spectrum. *Astrophys. J.* **703**, 675–691 (2009).
26. Xue, R. R. et al. Very high energy γ-ray afterglow emission of nearby gamma-ray bursts. *Astrophys. J.* **703**, 60–67 (2009).
27. Piran, T. & Nakar, E. On the external shock synchrotron model for gamma-ray bursts' GeV emission. *Astrophys. J. Lett.* **718**, 63–67 (2010).
28. Tam, P.-H. T., Tang, Q.-W., Hou, S.-J., Liu, R.-Y. & Wang, X.-Y. Discovery of an extra hard spectral component in the high-energy afterglow emission of GRB 130427A. *Astrophys. J. Lett.* **771**, 13 (2013).
29. Liu, R.-Y., Wang, X.-Y. & Wu, X.-F. Interpretation of the unprecedentedly long-lived high-energy emission of GRB 130427A. *Astrophys. J. Lett.* **773**, 20 (2013).
30. Ackermann, M. et al. Fermi-LAT observations of the gamma-ray burst GRB 130427A. *Science* **343**, 42–47 (2014).
31. Wang, X.-Y., Liu, R.-Y., Zhang, H.-M., Xi, S.-Q. & Zhang, B. Synchrotron self-Compton emission from afterglow shocks as the origin of the sub-TeV emission in GRB 180720B and GRB 190114C. *Astrophys. J.* **884**, 117–121 (2019)

MAGIC Collaboration*, P. Veres[1], P. N. Bhat[1,2], M. S. Briggs[1,2], W. H. Cleveland[3], R. Hamburg[1,2], C. M. Hui[4], B. Mailyan[1], R. D. Preece[1,2], O. J. Roberts[3], A. von Kienlin[5], C. A. Wilson-Hodge[4], D. Kocevski[4], M. Arimoto[6], D. Tak[7,8], K. Asano[9], M. Axelsson[10,11], G. Barbiellini[12], E. Bissaldi[13,14], F. Fana Dirirsa[15], R. Gill[16], J. Granot[16], J. McEnery[7,8], N. Omodei[17,18], S. Razzaque[15], F. Piron[19], J. L. Racusin[8], D. J. Thompson[8], S. Campana[20], M. G. Bernardini[20], N. P. M. Kuin[21], M. H. Siegel[22], S. B. Cenko[8,23], P. O'Brien[24], M. Capalbi[25], A. Dai[25], M. De Pasquale[26], J. Gropp[22], N. Klingler[22], J. P. Osborne[24], M. Perri[27,28], R. L. C. Starling[24], G. Tagliaferri[20,25], A. Tohuvavohu[22], A. Ursi[29], M. Tavani[29,30,31], M. Cardillo[29], C. Casentini[29], G. Piano[29], Y. Evangelista[29], F. Verrecchia[27,28], C. Pittori[27,28], F. Lucarelli[27,28], A. Bulgarelli[28], N. Parmiggiani[28], G. E. Anderson[32], J. P. Anderson[33], G. Bernardi[34,35,36], J. Bolmer[5], M. D. Caballero-García[37], I. M. Carrasco[38], A. Castellón[39], N. Castro Segura[40], A. J. Castro-Tirado[41,42], S. V. Cherukuri[43], A. M. Cockeram[44], P. D'Avanzo[20], A. Di Dato[45,46], R. Diretse[47], R. P. Fender[48], E. Fernández-García[42], J. P. U. Fynbo[49,50], A. S. Fruchter[51], J. Greiner[5], M. Gromadzki[52], K. E. Heintz[53], I. Heywood[35,48], A. J. van der Horst[54,55], Y.-D. Hu[42,56], C. Inserra[57], L. Izzo[42,58], V. Jaiswal[43], P. Jakobsson[53], J. Japelj[59], E. Kankare[60], D. A. Kann[42], C. Kouveliotou[54,55], S. Klose[61], A. J. Levan[62], X. Y. Li[63,64], S. Lotti[29], K. Maguire[65], D. B. Malesani[49,50,58,66], I. Manulis[67], M. Marongiu[68,69], S. Martin[33,70], A. Melandri[20], M. J. Michałowski[71], J. C. A. Miller-Jones[32], K. Misra[72,73], A. Moin[74], K. P. Mooley[75,76], S. Nasri[74], M. Nicholl[77,78], A. Noschese[45], G. Novara[79,80], S. B. Pandey[72], E. Peretti[68,81], C. J. Pérez del Pulgar[41], M. A. Pérez-Torres[42,82], D. A. Perley[44], L. Piro[29], F. Ragosta[46,83,84], L. Resmi[43], R. Ricci[34], A. Rossi[85], R. Sánchez-Ramírez[29], J. Selsing[50], S. Schulze[86], S. J. Smartt[87], I. A. Smith[88], V. V. Sokolov[89], J. Stevens[90], N. R. Tanvir[24], C. C. Thöne[42], A. Tiengo[79,80,91], E. Tremou[92], E. Troja[8,93], A. de Ugarte Postigo[42,58], A. F. Valeev[89], S. D. Vergani[94], M. Wieringa[95], P. A. Woudt[47], D. Xu[96], O. Yaron[67] & D. R. Young[87]

MAGIC Collaboration*

V. A. Acciari[97], S. Ansoldi[98,99], L. A. Antonelli[100], A. Arbet Engels[101], D. Baack[102], A. Babić[103], B. Banerjee[104], U. Barres de Almeida[105], J. A. Barrio[106], J. Becerra González[97], W. Bednarek[107], L. Bellizzi[108], E. Bernardini[109,110], A. Berti[111], J. Besenrieder[112], W. Bhattacharyya[109], C. Bigongiari[100], A. Biland[101], O. Blanch[113], G. Bonnoli[108], Ž. Bošnjak[103], G. Busetto[110], R. Carosi[114], G. Ceribella[112], Y. Chai[112], A. Chilingaryan[115], S. Cikota[103], S. M. Colak[113], U. Colin[112], E. Colombo[1], J. L. Contreras[106], J. Cortina[116], S. Covino[100], V. D'Elia[100], P. Da Vela[114], F. Dazzi[100], A. De Angelis[110], B. De Lotto[98], M. Delfino[113,117], J. Delgado[113,117], D. Depaoli[111], F. Di Pierro[111], L. Di Venere[111], E. Do Souto Espiñeira[113], D. Dominis Prester[118], A. Donini[98], D. Dorner[119], M. Doro[110], D. Elsaesser[102], V. Fallah Ramazani[120], A. Fattorini[102], G. Ferrara[100], D. Fidalgo[106], L. Foffano[110], M. V. Fonseca[106], L. Font[121], C. Fruck[112], S. Fukami[122], R. J. García López[1], M. Garczarczyk[109], S. Gasparyan[123], M. Gaug[121], N. Giglietto[111], F. Giordano[111], N. Godinović[124], D. Green[112], D. Guberman[113], D. Hadasch[122], A. Hahn[112], J. Herrera[1], J. Hoang[106], D. Hrupec[125], M. Hütten[112], T. Inada[122], S. Inoue[126], K. Ishio[112], Y. Iwamura[122], L. Jouvin[113], D. Kerszberg[113], H. Kubo[99], J. Kushida[127], A. Lamastra[100], D. Lelas[124], F. Leone[100], E. Lindfors[120], S. Lombardi[100], F. Longo[98,128,129], M. López[106], R. López-Coto[110], A. López-Oramas[1], S. Loporchio[111], B. Machado de Oliveira Fraga[105], C. Maggio[121], P. Majumdar[104], M. Makariev[130], M. Mallamaci[110], G. Maneva[130], M. Manganaro[118], K. Mannheim[119], L. Maraschi[100], M. Mariotti[110], M. Martínez[113], D. Mazin[112,122], S. Mićanović[118], D. Miceli[98], M. Minev[130], J. M. Miranda[108], R. Mirzoyan[112], E. Molina[131], A. Moralejo[113], D. Morcuende[106], V. Moreno[121], E. Moretti[113], P. Munar-Adrover[121], V. Neustroev[132], C. Nigro[109], K. Nilsson[120], D. Ninci[113], K. Nishijima[127], K. Noda[122], L. Nogués[113], S. Nozaki[99], S. Paiano[110], M. Palatiello[98], D. Paneque[112], R. Paoletti[108], J. M. Paredes[131], P. Peñil[106], M. Peresano[98], M. Persic[98], P. G. Prada Moroni[114], E. Prandini[110], I. Puljak[124], W. Rhode[102], M. Ribó[131], J. Rico[113], C. Righi[100], A. Rugliancich[114], L. Saha[106], N. Sahakyan[123], T. Saito[122], S. Sakurai[122], K. Satalecka[109], K. Schmidt[102], T. Schweizer[112], J. Sitarek[107], I. Šnidarić[133], D. Sobczynska[107], A. Somero[1], A. Stamerra[4], D. Strom[112], M. Strzys[112], Y. Suda[112], T. Surić[133], M. Takahashi[122], F. Tavecchio[4], P. Temnikov[130], T. Terzić[118,133], M. Teshima[112,122], N. Torres-Albà[131], L. Tosti[111], V. Vagelli[111], J. van Scherpenberg[112], G. Vanzo[1], M. Vazquez Acosta[1], C. F. Vigorito[111], V. Vitale[111], I. Vovk[112], M. Will[112], D. Zarić[124] & L. Nava[4,129,12]

[1]Center for Space Plasma and Aeronomic Research, University of Alabama in Huntsville, Huntsville, AL, USA. [2]Space Science Department, University of Alabama in Huntsville, Huntsville, AL, USA. [3]Science and Technology Institute, Universities Space Research Association, Huntsville, AL, USA. [4]Astrophysics Branch, ST12, NASA/Marshall Space Flight Center, Huntsville, AL, USA. [5]Max-Planck Institut für extraterrestrische Physik, Garching, Germany. [6]Faculty of Mathematics and Physics, Institute of Science and Engineering, Kanazawa University, Kanazawa, Japan. [7]Department of Physics, University of Maryland, College Park, MD, USA. [8]Astrophysics Science Division, NASA Goddard Space Flight Center, Greenbelt, MD, USA. [9]Institute for Cosmic-Ray Research, University of Tokyo, Kashiwa, Japan. [10]Department of Physics, Stockholm University, Stockholm, Sweden. [11]Department of Physics, KTH Royal Institute of Technology, Stockholm, Sweden. [12]Istituto Nazionale Fisica Nucleare (INFN), Trieste, Italy. [13]Dipartimento di Fisica "M. Merlin" dell'Università e del Politecnico di Bari, Bari, Italy. [14]Istituto Nazionale di Fisica Nucleare, Sezione di Bari, Bari, Italy. [15]Department of Physics, University of Johannesburg, Auckland Park, South Africa. [16]Department of Natural Sciences, Open University of Israel, Ra'anana, Israel. [17]W. W. Hansen Experimental Physics Laboratory, Kavli Institute for Particle Astrophysics and Cosmology, Department of Physics Stanford, Stanford, CA, USA. [18]SLAC National Accelerator Laboratory, Stanford University, Stanford, CA, USA. [19]Laboratoire Univers et Particules de Montpellier, Université Montpellier, CNRS/IN2P3, Montpellier, France. [20]INAF, Astronomical Observatory of Brera, Merate, Italy. [21]Mullard Space Science Laboratory, University College London, Dorking, UK. [22]Department of Astronomy and Astrophysics, Pennsylvania State University, University Park, PA, USA. [23]Joint Space-Science Institute, University of Maryland, College Park, MD, USA. [24]Department of Physics and Astronomy, University of Leicester, Leicester, UK. [25]INAF Istituto di Astrofisica Spaziale e Fisica Cosmica di Palermo, Palermo, Italy. [26]Department of Astronomy and Space Sciences, Istanbul University, Istanbul, Turkey. [27]INAF, Osservatorio Astronomico di Roma, Rome, Italy. [28]Space Science Data Center (SSDC), Agenzia Spaziale Italiana (ASI), Rome, Italy. [29]INAF-IAPS, Rome, Italy. [30]Università "Tor Vergata", Rome, Italy. [31]Gran Sasso Science Institute, L'Aquila, Italy. [32]International Centre for Radio Astronomy Research, Curtin University, Perth, Western Australia, Australia. [33]European Southern Observatory, Santiago, Chile. [34]INAF Istituto di Radioastronomia, Bologna, Italy. [35]Department of Physics and Electronics, Rhodes University, Grahamstown, South Africa. [36]South African Radio Astronomy Observatory, Cape Town, South Africa. [37]Astronomical Institute of the Academy of Sciences, Prague, Czech Republic. [38]Departamento de Física Aplicada, Facultad de Ciencias, Universidad de Málaga, Málaga, Spain. [39]Departamento de Álgebra, Geometría y Topología, Facultad de Ciencias, Universidad de Málaga, Málaga, Spain. [40]Physics and Astronomy Department, University of Southampton, Southampton, UK. [41]Unidad Asociada al CSIC Departamento de Ingeniería de Sistemas y Automática, E.T.S. de Ingenieros Industriales, Universidad de Málaga, Málaga, Spain. [42]Instituto de Astrofísica de Andalucía (IAA-CSIC), Granada, Spain. [43]Indian Institute of Space Science & Technology, Trivandrum, India. [44]Astrophysics Research Institute, Liverpool John Moores University, Liverpool, UK. [45]Osservatorio Astronomico 'S. Di Giacomo' AstroCampania, Agerola, Italy. [46]INAF - Astronomical Observatory of Naples, Naples, Italy. [47]Inter-University Institute for Data-Intensive Astronomy, Department of Astronomy, University of Cape Town, Rondebosch, South Africa. [48]Department of Physics, University of Oxford, Keble Road, Oxford, UK. [49]Cosmic Dawn Center (DAWN), Copenhagen, Denmark. [50]Niels Bohr Institute, Copenhagen University, Copenhagen, Denmark. [51]Space Telescope Science Institute, Baltimore, MD, USA. [52]Astronomical Observatory, University of Warsaw, Warsaw, Poland. [53]Centre for Astrophysics and Cosmology, Science Institute, University of Iceland, Reykjavik, Iceland. [54]Department of Physics, The George Washington University, Washington, DC, USA. [55]Astronomy, Physics, and Statistics Institute of Sciences (APSIS), The George Washington University, Washington, DC, USA. [56]Universidad de Granada, Facultad de Ciencias Campus Fuentenueva, Granada, Spain. [57]School of Physics & Astronomy, Cardiff University, Cardiff, UK. [58]DARK, Niels Bohr Institute, University of Copenhagen, Copenhagen, Denmark. [59]Anton Pannekoek Institute for Astronomy, University of Amsterdam, Amsterdam, The Netherlands. [60]Tuorla Observatory, Department of Physics and Astronomy, University of Turku, Turku, Finland. [61]Thüringer Landessternwarte Tautenburg, Tautenburg, Germany. [62]Department of Astrophysics/IMAPP, Radboud University, Nijmegen, The Netherlands. [63]Instituto de Hortofruticultura Subtropical y Mediterránea La Mayora (IHSM/UMA-CSIC), Málaga, Spain. [64]Nanjing Institute for Astronomical Optics and Technology, National Observatories, Chinese Academy of Sciences, Nanjing, China. [65]School of Physics, Trinity College Dublin, Dublin, Ireland. [66]DTU Space, National Space Institute, Technical University of Denmark, Kongens Lyngby, Denmark. [67]Benoziyo Center for Astrophysics, Weizmann Institute of Science, Rehovot, Israel. [68]Department of Physics and Earth Science, University of Ferrara, Ferrara, Italy. [69]International Center for Relativistic Astrophysics Network (ICRANet), Pescara, Italy. [70]Joint ALMA Observatory, Santiago, Chile. [71]Astronomical Observatory Institute, Faculty of Physics, Adam Mickiewicz University, Poznan, Poland. [72]Aryabhatta Research Institute of Observational Sciences, Nainital, India. [73]Department of Physics, University of California, Davis, CA, USA. [74]Physics Department, United Arab Emirates University, Al-Ain, United Arab Emirates. [75]National Radio Astronomy Observatory, Socorro, NM, USA. [76]Caltech, Pasadena, CA, USA. [77]Institute for Astronomy, University of Edinburgh, Royal Observatory, Edinburgh, UK. [78]Birmingham Institute for Gravitational Wave Astronomy and School of Physics and Astronomy, University of Birmingham, Birmingham, UK. [79]Scuola Universitaria Superiore IUSS

Pavia, Pavia, Italy. [80]INAF – IASF Milano, Milan, Italy. [81]INFN, Laboratori Nazionali del Gran Sasso, Assergi, Italy. [82]Departamento de Física Teórica, Universidad de Zaragoza, Zaragoza, Spain. [83]Dipartimento di Scienze Fisiche, Università degli studi di Napoli Federico II, Naples, Italy. [84]INFN Sezione di Napoli, Complesso Universitario di Monte S. Angelo, Naples, Italy. [85]INAF Osservatorio di Astrofisica e Scienza dello Spazio, Bologna, Italy. [86]Department of Particle Physics and Astrophysics, Weizmann Institute of Science, Rehovot, Israel. [87]Astrophysics Research Centre, School of Mathematics and Physics, Queen's University Belfast, Belfast, UK. [88]Department of Physics and Astronomy, Rice University, Houston, TX, USA. [89]Special Astrophysical Observatory (SAO-RAS), Nizhniy Arkhyz, Russia. [90]CSIRO Australia Telescope National Facility, Paul Wild Observatory, Narrabri, New South Wales, Australia. [91]Istituto Nazionale di Fisica Nucleare, Sezione di Pavia, Pavia, Italy. [92]AIM, CEA, CNRS, Université Paris Diderot, Sorbonne Paris Cité, Université Paris-Saclay, Gif-sur-Yvette, France. [93]Department of Astronomy, University of Maryland, College Park, MD, USA. [94]GEPI, Observatoire de Paris, PSL University, CNRS, Meudon, France. [95]Australia Telescope National Facility, CSIRO Astronomy and Space Science, Epping, New South Wales, Australia. [96]CAS Key Laboratory of Space Astronomy and Technology, National Astronomical Observatories, Chinese Academy of Sciences, Beijing, 100012, China. [97]Instituto de Astrofísica de Canarias and Departamento Astrofísica, Universidad de La Laguna, La Laguna, Spain. [98]Università di Udine and INFN Trieste, Udine, Italy. [99]Japanese MAGIC Consortium, Department of Physics, Kyoto University, Kyoto, Japan. [100]National Institute for Astrophysics (INAF), Rome, Italy. [101]ETH Zurich, Zurich, Switzerland. [102]Technische Universität Dortmund, Dortmund, Germany. [103]Croatian Consortium, University of Zagreb, FER, Zagreb, Croatia. [104]Saha Institute of Nuclear Physics, HBNI, Kolkata, India. [105]Centro Brasileiro de Pesquisas Físicas (CBPF), Rio de Janeiro, Brazil. [106]IPARCOS Institute and EMFTEL Department, Universidad Complutense de Madrid, Madrid, Spain. [107]University of Łódź, Department of Astrophysics, Łódź, Poland. [108]Università di Siena and INFN Pisa, Siena, Italy. [109]Deutsches Elektronen-Synchrotron (DESY), Zeuthen, Germany. [110]Università di Padova and INFN, Padua, Italy. [111]Istituto Nazionale Fisica Nucleare (INFN), Frascati, Italy. [112]Max-Planck-Institut für Physik, Munich, Germany. [113]Institut de Física d'Altes Energies (IFAE), The Barcelona Institute of Science and Technology (BIST), Barcelona, Spain. [114]Università di Pisa and INFN Pisa, Pisa, Italy. [115]The Armenian Consortium, A. Alikhanyan National Laboratory, Yerevan, Armenia. [116]Centro de Investigaciones Energéticas, Medioambientales y Tecnológicas, Madrid, Spain. [117]Port d'Informació Científica (PIC), Barcelona, Spain. [118]Croatian Consortium, Department of Physics, University of Rijeka, Rijeka, Croatia. [119]Universität Würzburg, Würzburg, Germany. [120]Finnish MAGIC Consortium, Finnish Centre of Astronomy with ESO (FINCA), University of Turku, Turku, Finland. [121]Departament de Física and CERES-IEEC, Universitat Autònoma de Barcelona, Bellaterra, Spain. [122]Japanese MAGIC Consortium, ICRR, The University of Tokyo, Kashiwa, Japan. [123]The Armenian Consortium, ICRANet-Armenia at NAS RA, Yerevan, Armenia. [124]Croatian Consortium, University of Split, FESB, Split, Croatia. [125]Croatian Consortium, Josip Juraj Strossmayer University of Osijek, Osijek, Croatia. [126]Japanese MAGIC Consortium, RIKEN, Wako, Japan. [127]Japanese MAGIC Consortium, Tokai University, Hiratsuka, Japan. [128]Dipartimento di Fisica, Università di Trieste, Trieste, Italy. [129]Institute for Fundamental Physics of the Universe (IFPU), Trieste, Italy. [130]Institute for Nuclear Research and Nuclear Energy, Bulgarian Academy of Sciences, Sofia, Bulgaria. [131]Universitat de Barcelona, ICCUB, IEEC-UB, Barcelona, Spain. [132]Finnish MAGIC Consortium, Astronomy Research Unit, University of Oulu, Oulu, Finland. [133]Croatian Consortium, Rudjer Boskovic Institute, Zagreb, Croatia . *e-mail: contact.magic@mpp.mpg.de

Methods

Prompt-emission observations

On 14 January 2019, the prompt emission from GRB 190114C triggered several space instruments, including Fermi-GBM[32], Fermi-LAT[33], Swift-BAT[34], Super-AGILE[35], AGILE-MCAL[35], KONUS-Wind[36], INTEGRAL-SPI-ACS[37] and Insight-HXMT[38]. The prompt-emission light curves from AGILE, Fermi and Swift are shown in Fig. 1 and in Extended Data Fig. 1, where the trigger time T_0 refers to the BAT trigger time (20:57:03.19 UT). The prompt emission lasts for approximately 25 s, when the last flaring-emission episode ends. Nominally, T_{90} (that is, the time interval during which a fraction between 5% and 95% of the total emission is observed) is much longer (>100 s, depending on the instrument)[14], but it is clearly contaminated by the afterglow component (Fig. 1) and does not provide a good measure of the actual duration of the prompt emission. A more detailed study of the prompt emission phase is reported in ref. [14].

AGILE

AGILE (Astrorivelatore Gamma ad Immagini Leggero)[39] could observe GRB 190114C until $T_0 + 330$ s, before it became occulted by the Earth. GRB 190114C triggered the MCAL (Mini-CALorimeter) from $T_0 - 0.95$ s to $T_0 + 10.95$ s. The MCAL light-flux curve in Fig. 1 was produced using two different spectral models. From $T_0 - 0.95$ s to $T_0 + 1.8$ s, the spectrum is fitted by a power law with photon index $\Gamma_{ph} = -1.97^{+0.47}_{-0.70}$ ($dN/dE \propto E^{\Gamma_{ph}}$). From $T_0 + 1.8$ s to $T_0 + 5.5$ s the best-fit model is a broken power law with $\Gamma_{ph,1} = -1.87^{+0.54}_{-0.19}$, $\Gamma_{ph,2} = -2.63^{+0.07}_{-0.07}$ and break energy $E_b = 756^{+137}_{-159}$ keV. The total fluence in the 0.4–100 MeV energy range is $F = 1.75 \times 10^{-4}$ erg cm^{-2}. The Super-AGILE detector also detected the burst, but the large off-axis angle prevented any X-ray imaging of the burst and any spectral analysis. Extended Data Fig. 1a, d, e shows the GRB 190114C light curves acquired by the Super-AGILE detector (20–60 keV) and by the MCAL detector in the low- (0.4–1.4 MeV) and high-energy (1.4–100 MeV) bands.

Fermi-GBM

There are indications that at the time of the MAGIC observations some of the detectors were partially shadowed by the structural elements of the Fermi spacecraft that were not modelled in the response of the GBM (Gamma-ray Burst Monitor) detectors. This affects the low-energy part of the spectrum[40]. For this reason, out of caution we elected to exclude the energy channels below 50 keV. The spectra detected by Fermi-GBM[41] during the intervals $T_0 + 68$ s to $T_0 + 110$ s and $T_0 + 110$ s to $T_0 + 180$ s are best described by a power-law model with photon index $\Gamma_{ph} = -2.10 \pm 0.08$ and $\Gamma_{ph} = -2.05 \pm 0.10$, respectively (Figs. 2, 3). The 10–1,000-keV light curve in Extended Data Fig. 1c was constructed by summing photon counts for the bright NaI detectors.

Swift-BAT

The 15–350-keV mask-weighted light curve of the BAT (Burst Alert Telescope)[42] shows a multi-peaked structure that starts at $T_0 - 7$ s (Extended Data Fig. 1b). The 68–110 s and 110–180 s spectra shown in Figs. 2, 3 were derived from a joint XRT–BAT fit. The best-fitting parameters for the whole interval (68–180 s) are: column density, $N_H = (7.53^{+0.74}_{-1.74}) \times 10^{22}$ cm^{-2} at $z = 0.42$, in addition to the galactic value of 7.5×10^{19} cm^{-2}; low-energy photon index, $\Gamma_{ph,1} = -1.21^{+0.40}_{-1.26}$; high-energy spectral index, $\Gamma_{ph,2} = -2.19^{+0.39}_{-0.19}$; and peak energy $E_{pk} > 14.5$ keV. Errors are given at 90% confidence level.

Fermi-LAT

Fermi-LAT (Large Area Telescope)[43] detected a γ-ray counterpart since the prompt phase[33]. The burst left the LAT field of view at $T_0 + 150$ s and remained outside it until $T_0 + 8{,}600$ s. The light curve in the energy range 0.1–10 GeV is shown in Extended Data Fig. 1f. The LAT spectra in the time bins 68–110 s and 110–180 s (Figs. 2, 3) are described by a power law with pivot energies of 200 MeV and 500 MeV, photon indices $\Gamma_{ph}(68\text{–}110) = -2.02 \pm 0.95$ and $\Gamma_{ph}(110\text{–}180) = -1.69 \pm 0.42$, and normalization factors of $N_{0,68\text{–}110} = (2.02 \pm 1.31) \times 10^{-7}$ MeV^{-1} cm^{-2} s^{-1} and $N_{0,110\text{–}180} = (4.48 \pm 2.10) \times 10^{-8}$ MeV^{-1} cm^{-2} s^{-1}, respectively. In each time interval, the analysis was limited to the energy range in which photons were detected. The LAT light curve integrated in the energy range 0.1–1 GeV is shown in Fig. 1.

MAGIC

To analyse the data we used the standard MAGIC software[44] and followed the steps optimized for data taking under moderate moon illumination[45]. The spectral fitting was performed by a forward-folding method, assuming a simple power law for the intrinsic spectrum and taking into account the EBL effect, using the model of Domínguez et al.[46]. Extended Data Table 1 shows the fitting results for various time bins (the pivot energy is chosen to minimize the correlation between the normalization and photon index parameters). The data points shown in Figs. 2, 3 were obtained from the observed excess rates in estimated energy, the fluxes of which were evaluated in true energy (photon corrected energy by Monte Carlo simulation, after reconstruction and unfolding) using the effective time and a spill-over-corrected effective area obtained from the best fit.

The time-resolved analysis hints to a possible spectral evolution to softer values, although we cannot exclude that the photon indices are compatible with a constant value of about −2.5 up to 2,400 s. The signal and background in the considered time bins are both in the low-count Poisson regime. Therefore, the correct treatment of the MAGIC data provided here includes the use of Poisson statistics, as well as systematic errors. To estimate the main source of systematic errors—our imperfect knowledge of the absolute instrument calibration and the total atmospheric transmission—we vary the light scale in our Monte Carlo simulation, as suggested in previous studies[44]. The result is reported in the last two lines of Extended Data Table 1 and in Extended Data Fig. 2.

The systematic effects deriving from the choice of one particular EBL model were also studied. The analysis performed to obtain the time-integrated spectrum was repeated, employing three other models[47–49]. The contribution to the systematic error on the photon index caused by the uncertainty on the EBL model is $\sigma_\alpha = ^{+0.10}_{-0.13}$, which is smaller than the statistical error only (one standard deviation), as already seen in a previous work[10]. On the other hand, the contribution of the choice of the EBL model to the systematic error on the normalization factor is only partially at the same level of the statistical error (one standard deviation), $\sigma_N = ^{+0.30}_{-0.08} \times 10^{-8}$. The chosen EBL model returns a normalization factor that is lower than two of the other models and very close to the third one[47].

The MAGIC energy-flux light curve that is presented in Fig. 1 was obtained by integrating the best-fit spectral model of each time bin from 0.3 to 1 TeV, in the same manner as in a previous study[10]. The value of the fitted time constant reported here differs less than two standard deviations from the one previously reported[10]. The difference is due to the poor constraints on the spectral-fit parameters of the last time bin, which influences the light-curve fit.

X-ray afterglow observations

Swift/XRT. Swift-XRT (X-Ray Telescope) started observing 68 s after T_0. The source light curve[50] was taken from the Swift-XRT light-curve repository[51] and was converted into 1–10-keV flux (Fig. 1) through dedicated spectral fits. The combined XRT + BAT spectral fit in Figs. 2, 3 is described above.

XMM-Newton and NuSTAR. The XMM-Newton X-ray observatory and the Nuclear Spectroscopic Telescope Array (NuSTAR) started observing GRB 190114C under Director's Discretionary Time (DDT) Target of Opportunities 7.5 h and 22.5 h, respectively, after the burst. The XMM-Newton and NuSTAR absorption-corrected fluxes (Fig. 1) were derived by fitting the spectrum with XSPEC and with the same

power-law model, considering absorption in our Galaxy and at the redshift of the burst.

NIR, optical and UV afterglow observations

Light curves from the different instruments presented in this section are shown in Extended Data Fig. 3.

GROND. The Gamma-Ray burst Optical/Near-infrared Detector (GROND)[52] started observations 3.8 h after the GRB trigger, and the follow-up continued until 29 January 29 2019. Image reduction and photometry were carried out with standard IRAF tasks[53], as described in refs. [54,55]. JHK_s photometry was converted to AB magnitudes to provide a common flux system. The final photometry is given in Extended Data Table 2.

BOOTES and GTC. The CASANDRA-1 ultra-wide-field camera[56] at the BOOTES-1 station in ESAt/INTA-CEDEA (Huelva, Spain) took an image of the GRB 190114C location, starting at 20:57:18 UT (30 s exposure time) (Extended Data Fig. 4). The Gran Canarias Telescope (GTC), equipped with the OSIRIS spectrograph[57], started observations 2.6 h post-burst. The grisms R1000B and R2500I were used, covering the wavelength range 3,700–10,000 Å (600 s exposure time for each grism). The GTC detected a highly extinguished continuum, as well as Ca II H and K lines in absorption and [O II], H_β and [O III] in emission (see Extended Data Fig. 5), all roughly at the same redshift of $z = 0.4245 \pm 0.0005$ (ref. [58]). By comparing the derived rest-frame equivalent widths with ref. [59], GRB 190114C clearly shows higher than average, but not unprecedented, values.

HST. The Hubble Space Telescope (HST) imaged the afterglow and host galaxy of GRB 190114C on 11 February and 12 March 2019. HST observations clearly reveal that the host galaxy is spiral (Extended Data Fig. 4). A direct subtraction of the epochs of observations with the F850LP filter yields a faint residual close to the nucleus of the host (Extended Data Fig. 4). From the position of the residual we estimate that the burst originated within 250 pc of the host galaxy nucleus.

LT. The robotic 2-m Liverpool Telescope (LT)[60] slewed to the afterglow location at coordinated universal time (UTC) 2019-01-14 23:22:34 and on the second night from UTC 2019-01-15 19:32:10 and acquired images in the B, g, V, r, i and z bands (45 s exposure each on the first night and 60 s on the second; see Extended Data Table 3). Aperture photometry of the afterglow was performed using a custom IDL script with a fixed aperture radius of 1.5″. Photometric calibration was performed relative to stars from the Pan-STARRS1 catalogue[61].

NTT. The European Southern Observatory's (ESO) New Technology Telescope (NTT) observed the optical counterpart of GRB 190114C under the extended Public ESO Spectroscopic Survey for Transient Objects (ePESSTO) using the NTT/EFOSC2 instrument in imaging mode[62]. Observations started at 04:36:53 UT on 16 January 2019 with g, r, i and z Gunn filters. Image reduction was carried out by following the standard procedures[63].

OASDG. The 0.5-m remote telescope of the Osservatorio Astronomico 'S. Di Giacomo' (OASDG), located in Agerola (Italy), started observations in the optical RC band 0.54 h after the burst. The afterglow of GRB 190114C was clearly detected in all the images.

NOT. The Nordic Optical Telescope (NOT) observed the optical afterglow of GRB 190114C with the Alhambra Faint Object Spectrograph and Camera (AlFOSC) instrument. Imaging was obtained in the griz filters with 300-s exposures, starting at 14 January 2019 21:20:56 UT, 24 min after the BAT trigger. The normalized spectrum (Extended Data Fig. 5) reveals strong host interstellar absorption lines of Ca H and K and of Na I D, which provided a redshift of $z = 0.425$.

REM. The 60-cm robotic Rapid Eye Mount telescope (REM) performed optical and NIR observations with the ROS2 optical imager and the REMIR NIR camera[64]. Observations were performed starting about 3.8 h after the burst in the r and J bands and lasted about one hour.

Swift/UVOT. The Swift UltraViolet and Optical Telescope (UVOT)[65] began observations at $T_0 + 54$ s in the UVOT v-band. The first observation after settling was in the UVOT white band[66], started 74 s after the trigger and lasted for 150 s. A 50-s exposure with the UV grism was taken next, followed by multiple exposures rotating through all seven broad- and intermediate-band filters, until switching to only the UVOT clear white filter on 20 January 2019. Standard photometric calibration and methods were used to derive the aperture photometry[67,68]. The grism zeroth-order data were reduced manually[69] to derive the B-magnitude and error.

VLT. The STARGATE collaboration used the Very Large Telescope (VLT) and observed GRB 190114C using the X-shooter spectrograph. Detailed analysis will be presented in forthcoming papers. A portion of the second spectrum is shown in Extended Data Fig. 5, illustrating the strong emission lines that are characteristic of a strongly star-forming galaxy, whose light is largely dominating over the afterglow at this epoch.

Magnitudes of the underlying galaxies

The HST images show a spiral or tidally disrupted galaxy whose bulge is coincident with the coordinates of GRB 190114C. A second galaxy is detected at an angular distance of 1.3″ towards the northeast. The SED analysis was performed with LePhare[70,71] using an iterative method that combined both the resolved photometry of the two galaxies found in the HST and VLT/HAWK-I data and the blended photometry from GALEX and WISE, in which the spatial resolution was much lower. Further details will be given in a separate paper (A.d.U.P. et al., manuscript in preparation). The estimated photometry for each object and their combination is given in Extended Data Table 4.

Optical extinction

The optical extinction towards the line of sight of a GRB is derived assuming a power law as the intrinsic spectral shape[72]. Once the Galactic extinction ($E_{B-V} = 0.01$; ref. [73]) is taken into account and the fairly bright host galaxy contribution is properly subtracted, a good fit to the data is obtained with the Large Magellanic Cloud recipe and $A_V = 1.83 \pm 0.15$. The spectral index β ($F_\nu \propto \nu^{\beta_O}$) evolves from hard to soft across the temporal break in the optical light curve at about 0.5 d, moving from $\beta_{O,1} = -0.10 \pm 0.12$ to $\beta_{O,2} = -0.48 \pm 0.15$.

Radio and submillimetre afterglow observations

The light curves obtained by the different instruments are shown in Extended Data Fig. 3.

ALMA. Observations with the Atacama Large Millimetre–Submillimetre Array (ALMA) are reported in Band 3 (central observed frequency of 97.500 GHz) and Band 6 (235.0487 GHz) between 15 January and 19 January 2019. The data were calibrated within CASA (Common Astronomy Software Applications; version 5.4.0)[74] using the pipeline calibration. Photometric measurements were also performed within CASA. Early ALMA observations at 97.5 GHz are taken from ref. [16].

ATCA. The Australia Telescope Compact Array (ATCA) observations were made with the ATCA 4-cm receivers (band centres of 5.5 and 9 GHz), 15-mm receivers (band centres of 17 and 19 GHz) and 7-mm receivers (band centres of 43 and 45 GHz). The ATCA data (see Extended Data Table 5) were obtained using the CABB continuum mode[75] and were reduced with the software packages Miriad[76] and CASA[74] using standard techniques. The quoted errors are 1σ, which include the root-mean-square (r.m.s.) and Gaussian 1σ errors.

GMRT. The upgraded Giant Metre-wave Radio Telescope[77] (UGMRT) observed on 17 January 2019 13.44 UT (2.8 d after the burst) in band 5 (1,000–1,450 MHz) with 2,048 channels spread over 400 MHz. The GMRT detected a weak source with a flux density of 73 ± 17 μJy at the GRB position[78]. The flux should be considered as an upper limit, as the contribution from the host[79] has not been subtracted.

MeerKAT. The new MeerKAT radio observatory[80,81] observed on 15 and 18 January 2019, with DDT requested by the ThunderKAT Large Survey Project[82]. Both epoch measurements used 63 antennas and were carried out in the L-band, spanning 856 MHz and centred at 1,284 MHz. The MeerKAT flux estimation was done by finding and fitting the source with the software PyBDSF v.1.8.15[83]. Adding the r.m.s. noise in quadrature to the flux uncertainty leads to final flux measurements of 125 ± 14 μJy per beam on 15 January and 97 ± 16 μJy per beam on 18 January. The contribution from the host galaxy[79] has not been subtracted. Therefore, these measurements provide a maximum flux of the GRB.

JCMT SCUBA-2. Sub-millimetre observations (Extended Data Table 5) were performed simultaneously at 850 μm and 450 μm on three nights using the Submillimetre Common-User Bolometer Array 2 (SCUBA-2) continuum camera[84] on the James Clerk Maxwell Telescope (JCMT). GRB 190114C was not detected on any of the individual measurements. By combining all the SCUBA-2 continuum camera[84] observations, the r.m.s. background noise is 0.95 mJy per beam at 850 μm and 5.4 mJy per beam at 450 μm at 1.67 d after the burst trigger.

Prompt-emission model for the early-time MAGIC emission

In the standard picture the prompt sub-megaelectronvolt spectrum is explained as synchrotron radiation from relativistic accelerated electrons in the energy-dissipation region. The associated inverse Compton component is sensitive to the details of the dynamics: for example, in the internal shock model if the peak energy is initially very high and the inverse Compton component is suppressed owing to Klein–Nishina effects, the peak of the inverse Compton component may be delayed and become bright only at late times, when scattering occurs in the Thomson regime. Simulations showed that the magnetic fields required to produce the gigaelectronvolt–teraelectronvolt component are rather low[85], with $\varepsilon_B \approx 10^{-3}$. In this framework the contribution of the inverse Compton component to the observed flux at early times (62–90 s; see Extended Data Table 1) does not exceed ~20%. Alternatively, if the prompt emission originates in reprocessed photospheric emission, the early teraelectronvolt flux may arise from inverse Compton scattering of thermal photons by freshly heated electrons below the photosphere at low optical depths. Another possibility for the generation of teraelectronvolt photons might be the inverse Compton scattering of prompt megaelectronvolt photons by electrons in the external forward-shock region, where electrons are heated to an average Lorentz factor of order 10^4 at early times.

Afterglow model

Synchrotron and SSC radiation from electrons accelerated at the forward shock were modelled within the external-shock scenario[7,8,20,25,86]. The results of the modelling are overlaid with the data in Fig. 3 and Extended Data Figs. 6, 7.

We consider two types of power-law radial profiles $n(R) = n_0 R^{-s}$ for the external environment: $s = 0$ (homogeneous medium) and $s = 2$ (wind-like medium, typical of an environment shaped by the stellar wind of the progenitor). In the latter case, we define $n_0 = 3 \times 10^{35} A_* \,\mathrm{cm}^{-1}$, where A_* is a parameter characterizing the normalization of the density. We assume that electrons swept up by the shock are accelerated into a power-law distribution described by the spectral index p, where $\mathrm{d}N/\mathrm{d}\gamma \propto \gamma^{-p}$, where γ is the electron Lorentz factor. We call ν_m the characteristic synchrotron frequency of electrons with Lorentz factor γ_m, ν_c is the cooling frequency and ν_{sa} the synchrotron self-absorption frequency.

The early-time optical emission (up to ~1,000 s) and radio emission (up to ~10^5 s) are probably dominated by reverse-shock radiation[16]. The detailed modelling of this component is not discussed here, where we focus on forward-shock radiation.

The XRT flux (Fig. 1, blue data points) decays as $F_X \propto t^{\alpha_X}$ with $\alpha_X = -1.36 \pm 0.02$. If $\nu_X > \max(\nu_m, \nu_c)$, the X-ray light curve is predicted to decay as $t^{(2-3p)/4}$, which implies $p \approx 2.5$. Another possibility is to assume $\nu_m < \nu_X < \nu_c$, which implies $p = 2.1$–2.2 for $s = 2$ and $p \approx 2.8$ for $s = 0$. A broken power law provides a better fit (5.3×10^{-5} probability of chance improvement), with a break occurring around 4×10^4 s and decay indices of $\alpha_{X,1} \approx -1.32 \pm 0.03$ and $\alpha_{X,2} \approx -1.55 \pm 0.04$. This behaviour can be explained by the passage of ν_c in the XRT band and assuming again $p = 2.4$–2.5 for $s = 2$ and $p \approx 2.8$ for $s = 0$.

The optical light curve starts displaying a shallow decay with time (with temporal index poorly constrained, between −0.5 and −0.25) starting from ~2×10^3 s, followed by a steepening around 8×10^4 s, when the temporal decay becomes similar to the decay in the X-ray band, which suggests that after this time the X-ray and optical bands lie in the same part of the synchrotron spectrum. If the break is interpreted as the synchrotron characteristic frequency ν_m crossing the optical band, after the break the observed temporal decay requires a steep value of $p \approx 3$ for $s = 0$ and a value between $p = 2.4$ and $p = 2.5$ for $s = 2$. Independently of the density profile of the external medium and of the cooling regime of the electrons, $\nu_m \propto t^{-3/2}$, which implies that ν_m is in the soft-X-ray band at 10^2 s. The SED at ~100 s is indeed characterized by a peak between 5–30 keV (Fig. 3). Information on the location of the self-absorption frequency is provided by observations at 1 GHz, showing that $\nu_{sa} \approx 1$ GHz at 10^5 s (Extended Data Fig. 6).

To summarize, in a wind-like scenario, X-ray and optical emission and their evolution in time can be explained if $p = 2.4$–2.5 and the emission is initially in the fast-cooling regime transitions to a slow-cooling regime around 3×10^3 s. The optical spectral index at late times is predicted to be $(1-p)/2 \approx -0.72$, in agreement with observations. ν_m crosses the optical band at $t \approx 8 \times 10^4$ s, explaining the steepening of the optical light curve and the flattening of the optical spectrum. The X-ray band initially lies above (or close to) ν_m, and the break frequency ν_c starts crossing the X-ray band around $(2$–$4) \times 10^4$ s, producing the steepening in the decay rate (the cooling frequency increases with time for $s = 2$). In this case, before the temporal break, the decay rate is related to the spectral index of the electron energy distribution by $\alpha_{X,1} = (2 - 3p)/4 \approx -1.3$ for $p \approx 2.4$–2.5. Well after the break, this value of p predicts a decay rate of $\alpha_{X,1} = (1 - 3p)/4$ between $\alpha_{X,1} = -1.55$ and $\alpha_{X,1} = -1.62$. Overall, this interpretation is also consistent with the fact that the late-time ($t > 10^5$ s) X-ray and optical light curves display similar temporal decays (Fig. 1), as they lie in the same part of the synchrotron spectrum ($\nu_m < \nu_{opt} < \nu_X < \nu_c$). A similar picture can be invoked to explain the emission when assuming a homogeneous density medium, but a steeper value of p is required. In this case, however, no break is predicted in the X-ray light curve.

We now add to the picture the information brought by the teraelectronvolt detection. The model is built with reference to the MAGIC flux and spectral indices derived considering statistical errors only (see Extended Data Table 1 and green data points in Extended Data Fig. 2). The light curve decays in time as $t^{-1.51}$ and the photon index is consistent within ~1σ with $\Gamma_{ph,TeV} \approx -2.5$ for the entire duration of the emission, although there is evidence for an evolution from stronger (about −2) to weaker (about −2.8) values. In the first broadband SED (Fig. 3, 68–110 s), LAT observations provide strong evidence for the presence of two separated spectral peaks.

Assuming Thomson scattering, the SSC peak is given by:

$$\nu_{\mathrm{peak}}^{\mathrm{SSC}} \approx 2\gamma_e^2 \nu_{\mathrm{peak}}^{\mathrm{syn}} \quad (1)$$

whereas in the Klein–Nishina regime, the SSC peak should be located at:

$$h\nu_{\rm peak}^{\rm SSC} \approx \frac{2\gamma_{\rm e}\Gamma m_{\rm e}c^2}{1+z} \quad (2)$$

where $\gamma_{\rm e} = \min(\gamma_{\rm c}, \gamma_{\rm m})$. The synchrotron spectral peak is located at $E_{\rm peak}^{\rm syn} \approx 10$ keV and the peak of the SSC component must be $E_{\rm peak}^{\rm SSC} \lesssim 100$ GeV to explain the MAGIC photon index. Both the Klein–Nishina and Thomson scattering regimes imply that $\gamma_{\rm e} \lesssim 10^3$. This small value presents two problems: (i) if the bulk Lorentz factor Γ is larger than 150 (which is a necessary condition to avoid strong γ–γ opacity; see below), a small $\gamma_{\rm m}$ translates into a small efficiency of the electron acceleration, with $\varepsilon_{\rm e} < 0.05$; (ii) the synchrotron peak energy can be located at $E_{\rm peak}^{\rm syn} \approx 10$ keV only for $B\Gamma \gtrsim 10^5$ G. A large B and a small $\varepsilon_{\rm e}$ would make it difficult to explain the presence of a strong SSC emission. These calculations show that γ–γ opacity probably plays a role in shaping and softening the observed SSC spectra[31,87].

For a γ-ray photon with energy E_γ, the $\tau_{\gamma\gamma}$ opacity is:

$$\tau_{\gamma\gamma}(E_\gamma) = \sigma_{\gamma\gamma}(R/\Gamma)n_{\rm t}(E_\gamma) \quad (3)$$

where $n_{\rm t} = L_{\rm t}/(4\pi R^2 c\Gamma E_{\rm t})$ is the density of target photons in the comoving frame, $L_{\rm t}$ is the luminosity and $E_{\rm t} = (m_{\rm e}c^2)^2\Gamma^2/[E_\gamma(1+z)^2]$ is the energy of target photons in the observer frame (c, speed of light in vacuum). Target photons for photons of energy $E_\gamma = 0.2$–1 TeV and for $\Gamma \approx 120$–150 have energies in the range 4–30 keV. When γ–γ absorption is relevant, the emission from pairs can give a non-negligible contribution to the radiative output.

To properly model all the physical processes that shape the broadband radiation, we use a numerical code that solves the evolution of the electron distributions and derives the radiative output, taking into account the following processes: synchrotron and SSC losses, adiabatic losses, γ–γ absorption, emission from pairs and synchrotron self-absorption[88–91]. We find that for the parameters assumed in the proposed model (see below), the contribution from pairs to the emission is negligible.

The MAGIC photon index (Extended Data Table 1) and its evolution with time constrain the SSC peak energy to ≲1 TeV at the beginning of the observations (Extended Data Table 1). In general, the internal opacity decreases with time and Klein–Nishina effects become less relevant. A possible softening of the spectrum with time, as the one suggested by the observations, requires that the spectral peak decreases with time and moves below the MAGIC energy range. In the slow-cooling regime, the SSC peak evolves to higher frequencies for a wind-like medium and decreases very slowly ($\nu_{\rm peak}^{\rm SSC} \propto t^{-1/4}$) for a constant-density medium (both in the Klein–Nishina and Thomson regimes). In the fast-cooling regime the evolution is faster ($\nu_{\rm peak}^{\rm SSC} \propto t^{-1/2} - t^{-9/4}$, depending on the medium and regime).

We model the multi-band observations considering both $s = 0$ and $s = 2$. The results are shown in Fig. 3, Extended Data Figs. 6, 7, where model curves are overlaid with observations. The model curves shown in these figures are derived using the following parameters. For the model in Fig. 3 and in Extended Data Figs. 7 (solid and dashed curves): $s = 0$, $\varepsilon_{\rm e} = 0.07$, $\varepsilon_{\rm B} = 8 \times 10^{-5}$, $p = 2.6$, $n_0 = 0.5$ and $E_{\rm k} = 8 \times 10^{53}$ erg. For the dotted curves in Extended Data Fig. 7 and the SEDs in Extended Data Fig. 6: $s = 2$, $\varepsilon_{\rm e} = 0.6$, $\varepsilon_{\rm B} = 10^{-4}$, $p = 2.4$, $A_* = 0.1$ and $E_{\rm k} = 4 \times 10^{53}$ erg.

Using the constraints on the afterglow onset time ($t_{\rm peak}^{\rm aft} \approx 5 - 10$ s, from the smooth component detected during the prompt emission) the initial bulk Lorentz factor is constrained to values $\Gamma_0 \approx 300$ and $\Gamma_0 \approx 700$ for $s = 2$ and $s = 0$, respectively.

Consistently with the qualitative description above, we find that late-time optical observations can indeed be explained with $\nu_{\rm m}$ crossing the band (see the SED modelling in Extended Data Fig. 6 and the dotted curves in Extended Data Fig. 7). However, a large $\nu_{\rm m}$ is required in this case and consequently the peak of the SSC component would also be large and lie above the MAGIC energy range. The resulting MAGIC light curve (green dotted curve in Extended Data Fig. 7) does not agree with observations. By relaxing the requirement on $\nu_{\rm m}$, the teraelectronvolt spectra (Fig. 3) and light curve (green solid curve in Extended Data Fig. 7) can be explained. As noted, a wind-like medium can explain the steepening of the X-ray light curve at 8×10^4 s, whereas no steepening is expected in a homogeneous medium (blue dotted and solid lines in Extended Data Fig. 7). We find that the gigaelectronvolt flux detected by LAT at a late time ($t \approx 10^4$ s) is dominated by the SSC component (dashed line in Extended Data Fig. 7).

Data availability

Data are available from the corresponding authors upon request.

Code availability

Proprietary data reconstruction codes were generated at the MAGIC telescope large-scale facility. Information supporting the findings of this study is available from the corresponding authors upon request. Source data for Figs. 2, 3 are provided with the paper.

32. Hamburg, R. GRB 190114C: Fermi GBM detection. *GCN Circulars* 23707 https://gcn.gsfc.nasa.gov/gcn3/23707.gcn3 (2019).
33. Kocevski, D. et al. GRB 190114C: Fermi-LAT detection. *GCN Circulars* 23709 https://gcn.gsfc.nasa.gov/gcn3/23709.gcn3 (2019).
34. Gropp, J. D. GRB 190114C: Swift detection of a very bright burst with a bright optical counterpart. *GCN Circulars* 23688 https://gcn.gsfc.nasa.gov/gcn3/23688.gcn3 (2019).
35. Ursi, A. et al. GRB 190114C: AGILE/MCAL detection. *GCN Circulars* 23712 https://gcn.gsfc.nasa.gov/gcn3/23712.gcn3 (2019).
36. Frederiks, D. et al. Konus-Wind observation of GRB 190114C. *GCN Circulars* 23737 https://gcn.gsfc.nasa.gov/gcn3/23737.gcn3 (2019).
37. Minaev, P. & Pozanenko, A. GRB 190114C: SPI-ACS/INTEGRAL extended emission detection. *GCN Circulars* 23714 https://gcn.gsfc.nasa.gov/gcn3/23714.gcn3 (2019).
38. Xiao, S. et al. GRB 190114C: Insight-HXMT/HE detection. *GCN Circulars* 23716 https://gcn.gsfc.nasa.gov/gcn3/23716.gcn3 (2019).
39. Tavani, M. et al. The AGILE mission. *Astron. Astrophys.* **502**, 995–1013 (2009).
40. Goldstein, A. et al. The Fermi GBM gamma-ray burst spectral catalog: the first two years. *Astrophys. J. Suppl. Ser.* **199**, 19 (2012).
41. Meegan, C. et al. The Fermi Gamma-ray Burst Monitor. *Astrophys. J.* **702**, 791–804 (2009).
42. Barthelmy, S. D. et al. The Burst Alert Telescope (BAT) on the SWIFT Midex Mission. *Space Sci. Rev.* **120**, 143–164 (2005).
43. Atwood, A. A. et al. The Large Area Telescope on the Fermi gamma-ray space telescope mission. *Astrophys. J.* **697**, 1071–1102 (2009).
44. Aleksić, J. et al. The major upgrade of the MAGIC telescopes, part II: a performance study using observations of the Crab Nebula. *Astropart. Phys.* **72**, 76–94 (2016).
45. Ahnen, M. L. et al. Performance of the MAGIC telescopes under moonlight. *Astropart. Phys.* **94**, 29–41 (2017).
46. Domínguez, A. et al. Extragalactic background light inferred from AEGIS galaxy-SED-type fractions. *Mon. Not. R. Astron. Soc.* **410**, 2556–2578 (2011).
47. Franceschini, A., Rodighiero, G. & Vaccari, M. Extragalactic optical-infrared background radiation, its time evolution and the cosmic photon-photon opacity. *Astron. Astrophys.* **487**, 837–852 (2008).
48. Finke, J. D., Razzaque, S. & Dermer, C. D. Modeling the extragalactic background light from stars and dust. *Astrophys. J.* **712**, 238–249 (2010).
49. Gilmore, R. C., Somerville, R. S., Primack, J. R. & Domínguez, A. Semi-analytic modelling of the extragalactic background light and consequences for extragalactic gamma-ray spectra. *Mon. Not. R. Astron. Soc.* **422**, 3189–3207 (2012).
50. UK Swift Science Data Centre. GRB 190114C Swift-XRT light curve https://www.swift.ac.uk/xrt_curves/00883832/.
51. Evans, P. A. et al. Methods and results of an automatic analysis of a complete sample of Swift-XRT observations of GRBs. *Mon. Not. R. Astron. Soc.* **397**, 1177–1201 (2009).
52. Greiner, J. et al. GROND—a 7-channel imager. *Publ. Astron. Soc. Pacif.* **120**, 405–424 (2008).
53. Tody, D. in *Astronomical Data Analysis Software and Systems II, ASP Conference Series* Vol. 52 (eds Hanisch, R. J. et al.) 173–183 (1993).
54. Krühler, T. et al. The 2175 Å dust feature in a gamma-ray burst afterglow at redshift 2.45. *Astrophys. J.* **685**, 376–383 (2008).
55. Bolmer, J. et al. Dust reddening and extinction curves toward gamma-ray bursts at $z > 4$. *Astron. Astrophys.* **609**, A62 (2018).
56. Castro-Tirado, A. J. et al. A very sensitive all-sky CCD camera for continuous recording of the night sky. In *Proc. SPIE, Advanced Software and Control for Astronomy II* Vol. 7019 (SPIE, 2008).
57. Cepa, J. et al. OSIRIS tunable imager and spectrograph. In In *Proc. SPIE Optical and IR Telescope Instrumentation and Detectors* Vol. 4008 (eds Iye, M. & Moorwood, A. F.) 623–631 (SPIE, 2000).
58. Castro-Tirado, A. GRB 190114C: refined redshift by the 10.4m GTC. *GCN Circulars* 23708 https://gcn.gsfc.nasa.gov/gcn3/23708.gcn3 (2019).

59. de Ugarte Postigo, A. et al. The distribution of equivalent widths in long GRB afterglow spectra. *Astron. Astrophys.* **548**, A11 (2012).
60. Steele, I. A. et al. The Liverpool Telescope: performance and first results. In *Proc. SPIE Ground-based Telescopes* Vol. 5489 (ed. Oschmann, J. M. Jr) 679–692 (SPIE, 2004).
61. Chambers, K. C. et al. The Pan-STARRS1 surveys. Preprint at https://arxiv.org/abs/1612.05560 (2016).
62. Tarenghi, M. & Wilson, R. N. The ESO NTT (New Technology Telescope): the first active optics telescope. In *Proc. SPIE Active Telescope Systems* Vol. 1114 (ed. Roddier, F. J.) 302–313 (SPIE, 1989).
63. Smartt, S. J. et al. PESSTO: survey description and products from the first data release by the Public ESO Spectroscopic Survey of Transient Objects. *Astron. Astrophys.* **579**, A40 (2015).
64. Covino, S. et al. REM: a fully robotic telescope for GRB observations. In *Proc. SPIE Ground-based Instrumentation for Astronomy* Vol. 5492 (eds Moorwood, A. F. M. & Iye, M.) 1613–1622 (SPIE, 2004).
65. Roming, P. W. A. et al. The Swift ultra-violet/optical telescope. *Space Sci. Rev.* **120**, 95–142 (2005).
66. Siegel, M. H. & Gropp, J. D. GRB 190114C: Swift/UVOT detection. *GCN Circulars* 23725 https://gcn.gsfc.nasa.gov/gcn3/23725.gcn3 (2019).
67. Poole, T. S. et al. Photometric calibration of the Swift ultraviolet/optical telescope. *Mon. Not. R. Astron. Soc.* **383**, 627–645 (2008).
68. Breeveld, A. A. et al. An updated ultraviolet calibration for the Swift/UVOT. In *American Institute of Physics Conference Series* Vol. 1358, 373–376 (AIP, 2011).
69. Kuin, N. P. M. et al. Calibration of the Swift-UVOT ultraviolet and visible grisms. *Mon. Not. R. Astron. Soc.* **449**, 2514–2538 (2015).
70. Arnouts, S. et al. Measuring and modelling the redshift evolution of clustering: the Hubble Deep Field North. *Mon. Not. R. Astron. Soc.* **310**, 540–556 (1999).
71. Ilbert, O. et al. Accurate photometric redshifts for the CFHT legacy survey calibrated using the VIMOS VLT deep survey. *Astron. Astrophys.* **457**, 841–856 (2006).
72. Covino, S. et al. Dust extinctions for an unbiased sample of gamma-ray burst afterglows. *Mon. Not. R. Astron. Soc.* **432**, 1231–1244 (2013).
73. Schlafly, E. F. & Finkbeiner, D. P. Measuring reddening with Sloan Digital Sky Survey stellar spectra and recalibrating SFD. *Astrophys. J.* **737**, 103 (2011).
74. McMullin, J. P., Waters, B., Schiebel, D., Young, W. & Golap, K. CASA architecture and applications. In *Astronomical Data Analysis Software and Systems XVI*, Vol. 376 (eds Shaw, R. A. et al.) 127 (ASP, 2007).
75. Wilson, W. E. et al. The Australia Telescope Compact Array broad-band backend: description and first results. *Mon. Not. R. Astron. Soc.* **416**, 832–856 (2011).
76. Sault, R. J., Teuben, P. J. & Wright, M. C. H. A retrospective view of MIRIAD. In *Astronomical Data Analysis Software and Systems IV* Vol. 77 (eds Shaw, R. A. et al.) 433 (ASP, 1995).
77. Swarup, G. et al. The Giant Metre-wave Radio Telescope. *Current Science* **60**, 95–105 (1991).
78. Cherukuri, S. V. et al. GRB 190114C: GMRT detection at 1.26GHz. *GCN Circulars* 23762 https://gcn.gsfc.nasa.gov/gcn3/23762.gcn3 (2019).
79. Tremou, L. et al. GRB 190114C: MeerKAT radio observation. *GCN Circulars* 23760 https://gcn.gsfc.nasa.gov/gcn3/23760.gcn3 (2019).
80. Camilo, F. et al. Revival of the magnetar PSR J1622-4950: observations with MeerKAT, Parkes, XMM-Newton, Swift, Chandra, and NuSTAR. *Astrophys. J.* **856**, 180 (2018).
81. Jonas, J. L. & The MeerKAT Team. The MeerKAT Radio Telescope. In *Proc. of MeerKAT Science: On the Pathway to the SKA* 001 (2016).
82. Fender, R. et al. ThunderKAT: the MeerKAT large survey project for image-plane radio transients. Preprint at https://arxiv.org/abs/1711.04132 (2017).
83. Mohan, N. & Rafferty, D. PyBDSF: Python Blob Detection and Source Finder https://www.astron.nl/citt/pybdsf/ (2015)
84. Holland, W. S. et al. SCUBA-2: the 10 000 pixel bolometer camera on the James Clerk Maxwell Telescope. *Mon. Not. R. Astron. Soc.* **430**, 2513–2533 (2013).
85. Bošnjak, Ž., Daigne, F. & Dubus, G. Prompt high-energy emission from gamma-ray bursts in the internal shock model. *Astron. Astrophys.* **498**, 677–703 (2009).
86. Panaitescu, A. & Kumar, P. Analytic light curves of gamma-ray burst afterglows: homogeneous versus wind external media. *Astrophys. J.* **543**, 66–76 (2000).
87. Derishev, E. & Piran, T. The physical conditions of the afterglow implied by MAGIC's sub-TeV observations of GRB 190114C. *Astrophys. J. Lett.* **880**, 27 (2019).
88. Mastichiadis, A. & Kirk, J. G. Self-consistent particle acceleration in active galactic nuclei. *Astron. Astrophys.* **295**, 613 (1995).
89. Vurm, I. & Poutanen, J. Time-dependent modeling of radiative processes in hot magnetized plasmas. *Astrophys. J.* **698**, 293–316 (2009).
90. Petropoulou, M. & Mastichiadis, A. On the multiwavelength emission from gamma ray burst afterglows. *Astron. Astrophys.* **507**, 599–610 (2009).
91. Pennanen, T., Vurm, I. & Poutanen, J. Simulations of gamma-ray burst afterglows with a relativistic kinetic code. *Astron. Astrophys.* **564**, A77 (2014).

Acknowledgements We thank the Instituto de Astrofísica de Canarias for the excellent working conditions at the Observatorio del Roque de los Muchachos in La Palma. We acknowledge financial support by the German BMBF and MPG, the Italian INFN and INAF, the Swiss National Fund SNF, the ERDF under the Spanish MINECO (FPA2017-87859-P, FPA2017-85668-P, FPA2017-82729-C6-2-R, FPA2017-82729-C6-6-R, FPA2017-82729-C6-5-R, AYA2015-71042-P, AYA2016-76012-C3-1-P, ESP2017-87055-C2-2-P, FPA201790566REDC), the Indian Department of Atomic Energy, the Japanese JSPS and MEXT, the Bulgarian Ministry of Education and Science, National RI Roadmap Project DO1-153/28.08.2018 and the Academy of Finland grant number 320045. This work was also supported by the Spanish Centro de Excelencia 'Severo Ochoa' through grants SEV-2016-0588 and SEV-2015-0548 and Unidad de Excelencia 'María de Maeztu' MDM-2014-0369, by the Croatian Science Foundation (HrZZ) Project IP-2016-06-9782 and the University of Rijeka Project 13.12.1.3.02, by the DFG Collaborative Research Centers SFB823/C4 and SFB876/C3, the Polish National Research Centre grant UMO-2016/22/M/ST9/00382 and by the Brazilian MCTIC, CNPq and FAPERJ. L. Nava acknowledges funding from the European Union's Horizon 2020 Research and Innovation programme under the Marie Skłodowska-Curie grant agreement number 664931. E. Moretti acknowledges funding from the European Union's Horizon 2020 research and innovation programme under Marie Skłodowska-Curie grant agreement number 665919. This study used the following ALMA data: ADS/JAO.ALMA#2018.A.00020.T, ADS/JAO.ALMA#2018.1.01410.T. ALMA is a partnership of ESO (representing its member states), NSF (USA) and NINS (Japan), together with NRC (Canada), MOST and ASIAA (Taiwan), and KASI (Republic of Korea), in cooperation with the Republic of Chile. The Joint ALMA Observatory is operated by ESO, AUI/NRAO and NAOJ. C.C.T., A.d.U.P. and D.A.K. acknowledge support from the Spanish research project AYA2017-89384-P. C.C.T and A.d.U.P. acknowledge support from funding associated with Ramón y Cajal fellowships (RyC-2012-09984 and RyC-2012-09975). D.A.K. acknowledges support from funding associated with Juan de la Cierva Incorporación fellowships (IJCI-2015-26153). The JCMT is operated by the East Asian Observatory on behalf of The National Astronomical Observatory of Japan, Academia Sinica Institute of Astronomy and Astrophysics, the Korea Astronomy and Space Science Institute, and Center for Astronomical Mega-Science (as well as the National Key R&D Program of China via grant number 2017YFA0402700). Additional funding support is provided by the Science and Technology Facilities Council of the UK and participating universities in the UK and Canada. The JCMT data reported here were obtained under project M18BP040 (principal investigator D.A.P.). We thank M. Rawlings, K. Silva, S. Urquart and the JCMT staff for support for these observations. The Liverpool Telescope, located on the island of La Palma, in the Spanish Observatorio del Roque de los Muchachos of the Instituto de Astrofisica de Canarias, is operated by Liverpool John Moores University with financial support from the UK Science and Technology Facilities Council. The Australia Telescope Compact Array is part of the Australia Telescope National Facility, which is funded by the Australian Government for operation as a National Facility managed by CSIRO. G.E.A. is the recipient of an Australian Research Council Discovery Early Career Researcher Award (project number DE180100346) and J.C.A.M.-J. is the recipient of an Australian Research Council Future Fellowship (project number FT140101082) funded by the Australian Government. Support for the German contribution to GBM was provided by the Bundesministerium für Bildung und Forschung (BMBF) via the Deutsches Zentrum für Luft und Raumfahrt (DLR) under grant number 50 QV 0301. The University of Alabama in Huntsville (UAH) coauthors acknowledge NASA funding from cooperative agreement NNM11AA01A. C.A.W.-H. and C.M.H. acknowledge NASA funding through the Fermi-GBM project. The Fermi LAT Collaboration acknowledges support from a number of agencies and institutes that have supported both the development and the operation of the LAT, as well as scientific data analysis. These include the National Aeronautics and Space Administration and the Department of Energy (DOE) in the USA; the Commissariat à l'Energie Atomique and the Centre National de la Recherche Scientifique/Institut National de Physique Nucléaire et de Physique des Particules in France; the Agenzia Spaziale Italiana and the Istituto Nazionale di Fisica Nucleare in Italy; the Ministry of Education, Culture, Sports, Science and Technology (MEXT), High Energy Accelerator Research Organization (KEK) and Japan Aerospace Exploration Agency (JAXA) in Japan; and the K. A. Wallenberg Foundation, the Swedish Research Council and the Swedish National Space Board in Sweden. We acknowledge additional support for science analysis during the operations phase from the Istituto Nazionale di Astrofisica in Italy and the Centre National d'Études Spatiales in France. This work was performed in part under DOE contract DE-AC02-76SF00515. Part of the funding for GROND (both hardware and personnel) was granted from the Leibniz-Prize to G. Hasinger (DFG grant HA 1850/28-1). Swift data were retrieved from the Swift archive at HEASARC/NASA-GSFC and from the UK Swift Science Data Centre. Support for Swift in the UK is provided by the UK Space Agency. This work is based on observations obtained with XMM-Newton, an ESA science mission with instruments and contributions directly funded by ESA Member States and NASA. This work is partially based on observations collected at the European Organisation for Astronomical Research in the Southern Hemisphere under ESO programme 199.D-0143. The work is partly based on observations made with the GTC, installed in the Spanish Observatorio del Roque de los Muchachos of the Instituto de Astrofísica de Canarias, in the island of La Palma. This work is partially based on observations made with the NOT (programme 58-502), operated by the Nordic Optical Telescope Scientific Association at the Observatorio del Roque de los Muchachos, La Palma, Spain, of the Instituto de Astrofísica de Canarias. This work is partially based on observations collected at the European Organisation for Astronomical Research in the Southern Hemisphere under ESO programme 102.D-0662. This work is partially based on observations collected through the ESO programme 199.D-0143 ePESSTO. M. Gromadzki is supported by the Polish NCN MAESTRO grant 2014/14/A/ST9/00121. M.N. is supported by a Royal Astronomical Society Research Fellowship M.G.B., S. Campana, A. Melandri and P.D'A. acknowledge ASI grant I/004/11/3. S. Campana acknowledges support from agreement ASI-INAF number 2017-14-H.0. S.J.S. acknowledges funding from STFC grant ST/P000312/1. N.P.M.K. acknowledges support by the UK Space Agency under grant ST/P002323/1 and the UK Science and Technology Facilities Council under grant ST/N00811/1. L.P. and S. Lotti acknowledge partial support from agreement ASI-INAF number 2017-14-H.0. A.F.V. acknowledges RFBR 18-29-21030 for support. A.J.C.-T. acknowledges support from the Junta de Andalucía (Project P07-TIC-03094) and from the Spanish Ministry Projects AYA2012-39727-C03-01 and 2015-71718R. K. Misra acknowledges support from the Department of Science and Technology (DST), Government of India and the Indo-US Science and Technology Forum (IUSSTF) for the WISTEMM fellowship and Departnment of Physics, UC Davis, where a part of this work was carried out. S.B.P. and K. Misra acknowledge BRICS (Brazil, Russia, India, China and South Africa) grant DST/IMRCD/BRICS/Pilotcall/ProFCheap/2017(G) for this work. M.J.M. acknowledges the support of the National Science Centre, Poland, through grant 2018/30/E/ST9/00208. V.J. and L.R. acknowledge support from grant EMR/2016/007127 from the Department of Science and Technology, India. K. Maguire acknowledges support from H2020 through an ERC starting grant (758638). L.I. acknowledges M. Della Valle for support in the operation of the telescope.

Author contributions The MAGIC telescope system was designed and constructed by the MAGIC Collaboration. Operation, data processing, calibration, Monte Carlo simulations of the detector and of theoretical models, and data analyses were performed by the members of the MAGIC Collaboration, who also discussed and approved the scientific results. L. Nava coordinated the collection of the data, developed the theoretical interpretation and wrote the main section and the section on afterglow modelling. E. Moretti coordinated the analysis of the MAGIC data, wrote the relevant sections and, together with F. Longo, coordinated the

collaboration with the Fermi team. D. Miceli, Y.S. and S.F. performed the analysis of the MAGIC data. S. Covino provided support with the analysis of the optical data and the writing of the corresponding sections. Z.B. performed calculations for the contribution of prompt emission to the teraelectronvolt radiation and wrote the corresponding section. A. Stamerra, D.P. and S.I. contributed to structuring and editing the paper. A. Berti contributed to editing and finalizing the manuscript. R.M. coordinated and supervised the writing of the paper. All MAGIC collaborators contributed to the editing of and provided comments on the final version of the manuscript. S. Campana and M.G.B. extracted the spectra and performed the spectral analysis of the Swift-BAT and Swift-XRT data. N.P.M.K. derived the photometry for the Swift-UVOT event mode data and the UV grism exposure. M.H.S. derived the image-mode Swift-UVOT photometry. A.d.U.P. was principal investigator of ALMA programme 2018.1A.00020.T, triggered these observations and performed photometry. S. Martin reduced the ALMA Band 6 data. C.C.T., S. Schulze, D.A.K. and M. Michałowski participated in the ALMA DDT proposal preparation, observations and scientific analysis of the data. D.A.P. was principal investigator of ALMA programme 2018.1.01410.T and triggered these observations and was principal investigator of the LT and JCMT programmes. A.M.C. analysed the ALMA Band 3 and LT data and wrote the LT text. S. Schulze contributed to the development of the ALMA Band 3 observing programme. I.A.S. triggered the JCMT programme, analysed the data and wrote the associated text. N.R.T. contributed to the development of the JCMT programme. D.A.K. and C.C.T. triggered and coordinated the X-shooter observations. D.A.K. independently checked the optical light curve analysis. K. Misra was the principal investigator of the GMRT programme 35_018. S.V.C. and V.J. analysed the data. L.R. contributed to the observation plan and data analysis. E. Tremou, I.H. and R.D. performed the MeerKAT data analysis. G.E.A., A. Moin, S. Schulze and E. Troja were principal investigators of ATCA programme CX424. G.E.A., M. Wieringa and J. Stevens carried out the observations. G.E.A., G. Bernardi, S.K., M. Marongiu, A. Moin, R.R. and M. Wieringa analysed these data. J.C.A.M.-J. and L.P. participated in the ATCA proposal preparation and the scientific analysis of the data. The ePESSTO project was delivered by the following, who contributed to managing, executing, reducing, analysing ESO/NTT data and provided comments to the manuscript: J.P.A., N.C.S., P.D'A., M. Gromadzki, C.I., E.K., K. Maguire, M.N., F.R. and S.J.S.; A. Melandri and A. Rossi reduced and analysed REM data and provided comments to the manuscript. J. Bolmer was responsible for observing the GRB with GROND and for the data reduction and calibration. J. Bolmer and J. Greiner contributed to the analysis of the data and writing of the text. E. Troja triggered the NuSTAR TOO observations performed under the DDT programme, L.P. requested the XMM-Newton data, obtained under a DDT programme, and carried out the scientific analysis of the XMM-Newton and NuSTAR data. S. Lotti analysed the NuSTAR data and wrote the associated text. A. Tiengo and G. Novara analysed the XMM-Newton data and wrote the associated text. A.J.C.-T. led the observing BOOTES and GTC programmes. A. Castellón, C.J.P.d.P., E.F.-G., I.M.C., S.B.P. and X.Y.L. analysed the BOOTES data, and A.F.V., M.D.C.-G., R.S.-R., Y.-D.H. and V.V.S. analysed the GTC data and interpreted them accordingly. N.R.T. created the X-shooter and AlFOSC figures. J.P.U.F. and J.J. performed the analysis of the X-shooter and AlFOSC spectra. D.X. and P.J. contributed to the NOT programme and triggering. D. Malesani performed photometric analysis of NOT data. E. Peretti contributed to the development of the code for modelling afterglow radiation. L.I. triggered and analysed the OASDG data, and A.D.D. and A.N. performed the observations at the telescope.

Competing interests The authors declare no competing interests.

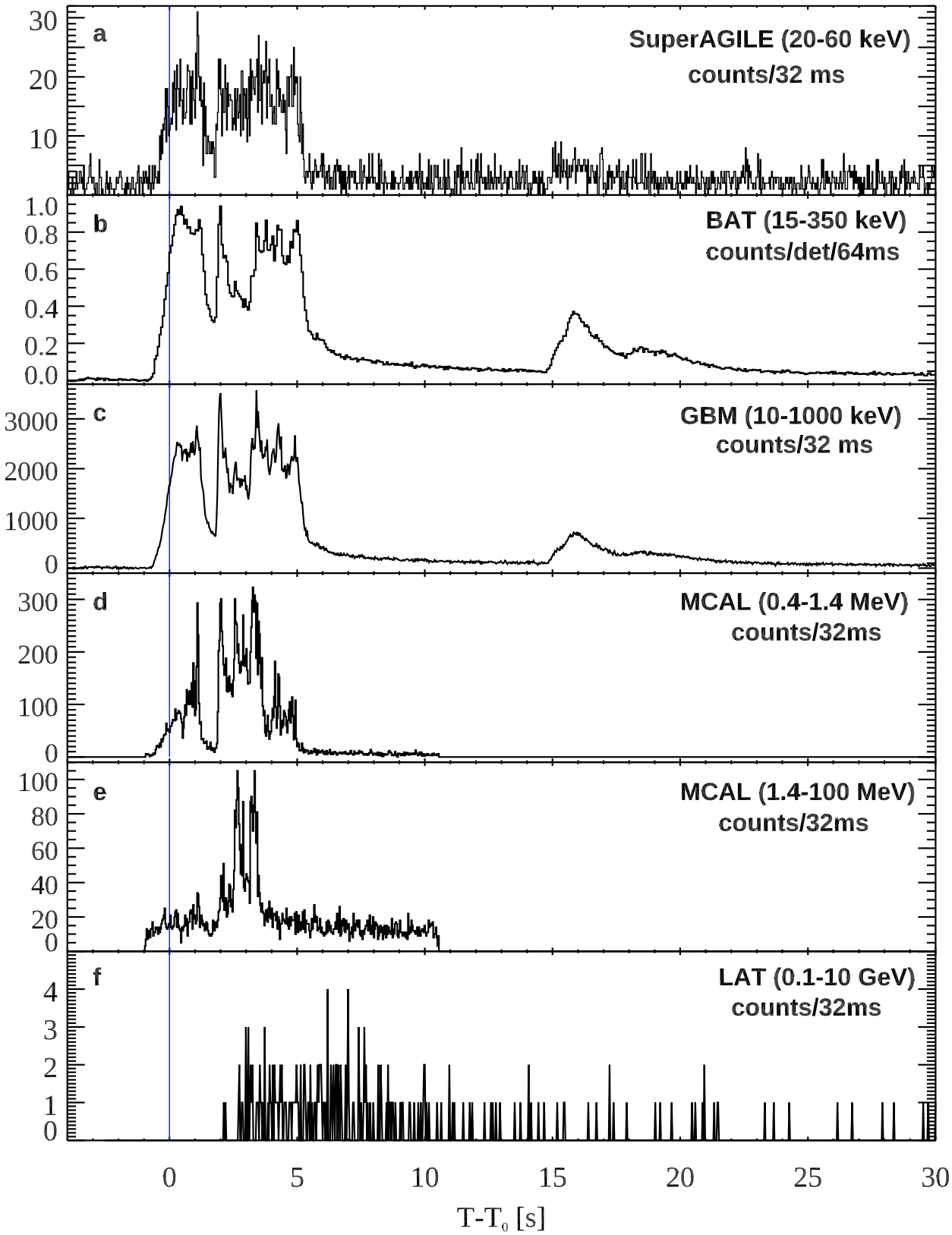

Extended Data Fig. 1 | Prompt-emission light curves for different detectors. **a**–**f**, Light curves for Super-AGILE (**a**; 20–60 keV), Swift-BAT (**b**; 15–150 keV), Fermi-GBM (**c**; 10–1,000 keV), AGILE-MCAL (**d**; 0.4–1.4 MeV), AGILE-MCAL (**e**; 1.4–100 MeV) and Fermi-LAT (**f**; 0.1–10 GeV). The light curve of AGILE-MCAL is split into two bands to show the energy dependence of the first peak. Error bars show 1σ statistical errors.

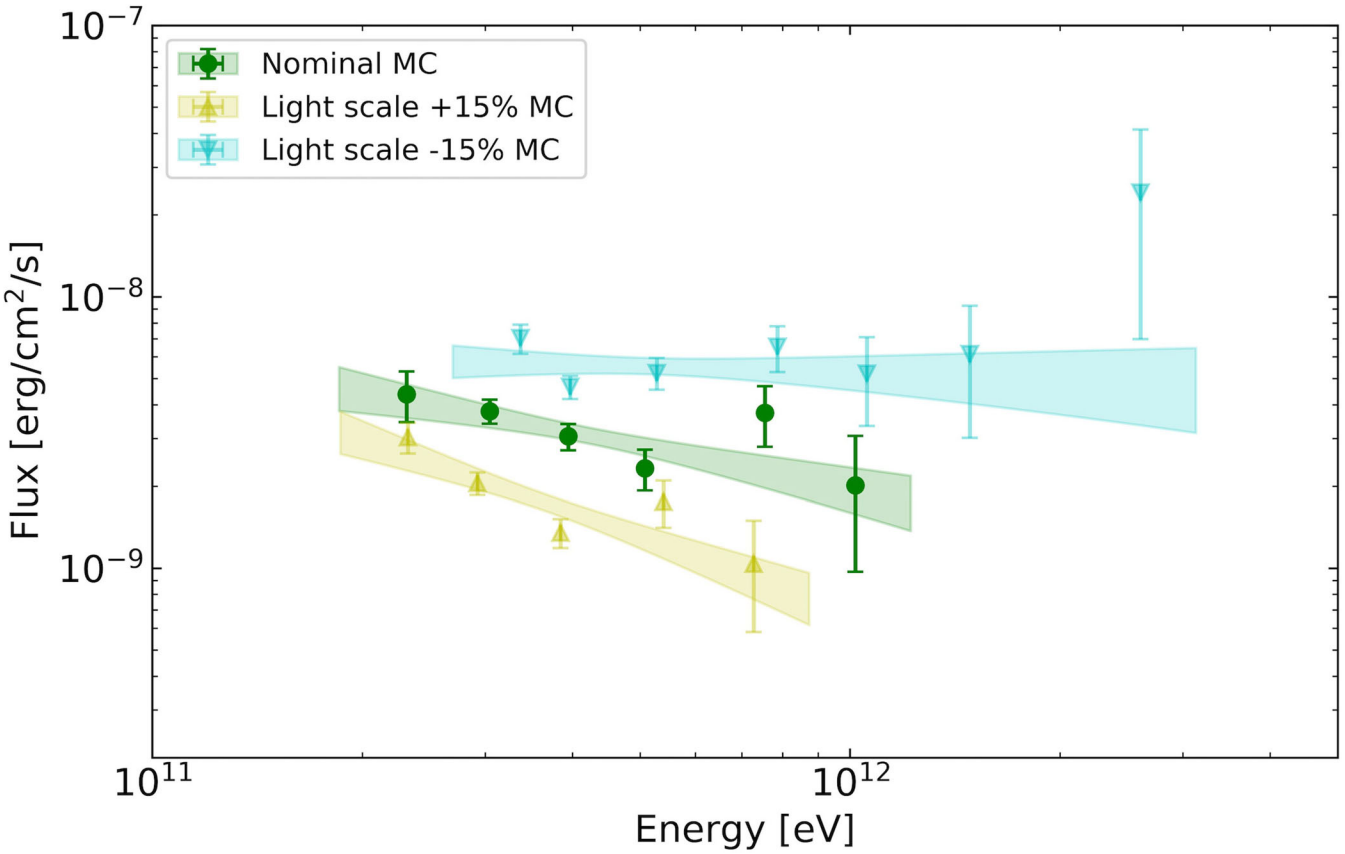

Extended Data Fig. 2 | MAGIC time-integrated SEDs in the time interval 62–2,400 s after T_0. The green (yellow, blue) points and band show the results of the Monte Carlo (MC) simulations for the nominal and the varied light scale cases (+15%, −15%), which define the limits of the systematic uncertainties. The contour regions are drawn from the 1σ error of their best-fit power-law functions. The vertical bars of the data points show the 1σ errors on the flux.

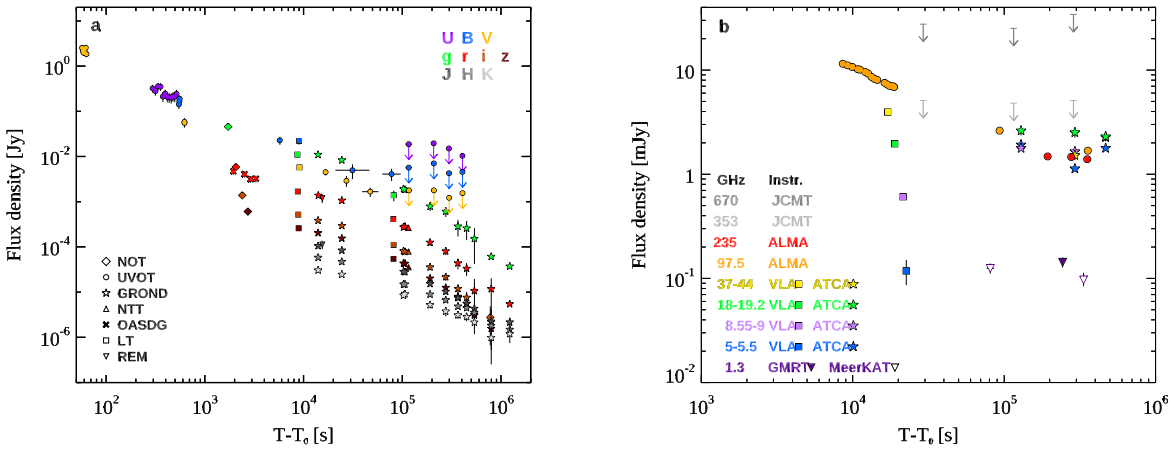

Extended Data Fig. 3 | Afterglow light curves of GRB 190114C. Flux density at different frequencies as a function of the time since the initial burst, $T-T_0$. **a**, Observation in the NIR, optical and UV bands. The flux has been corrected for extinction in the host and in our Galaxy. The contribution of the host galaxy and its companion has been subtracted. Fluxes have been rescaled (except for the r-band filter). **b**, Radio and submillimetre observations from 1.3 GHz to 670 GHz. 'Instr.', instrument.

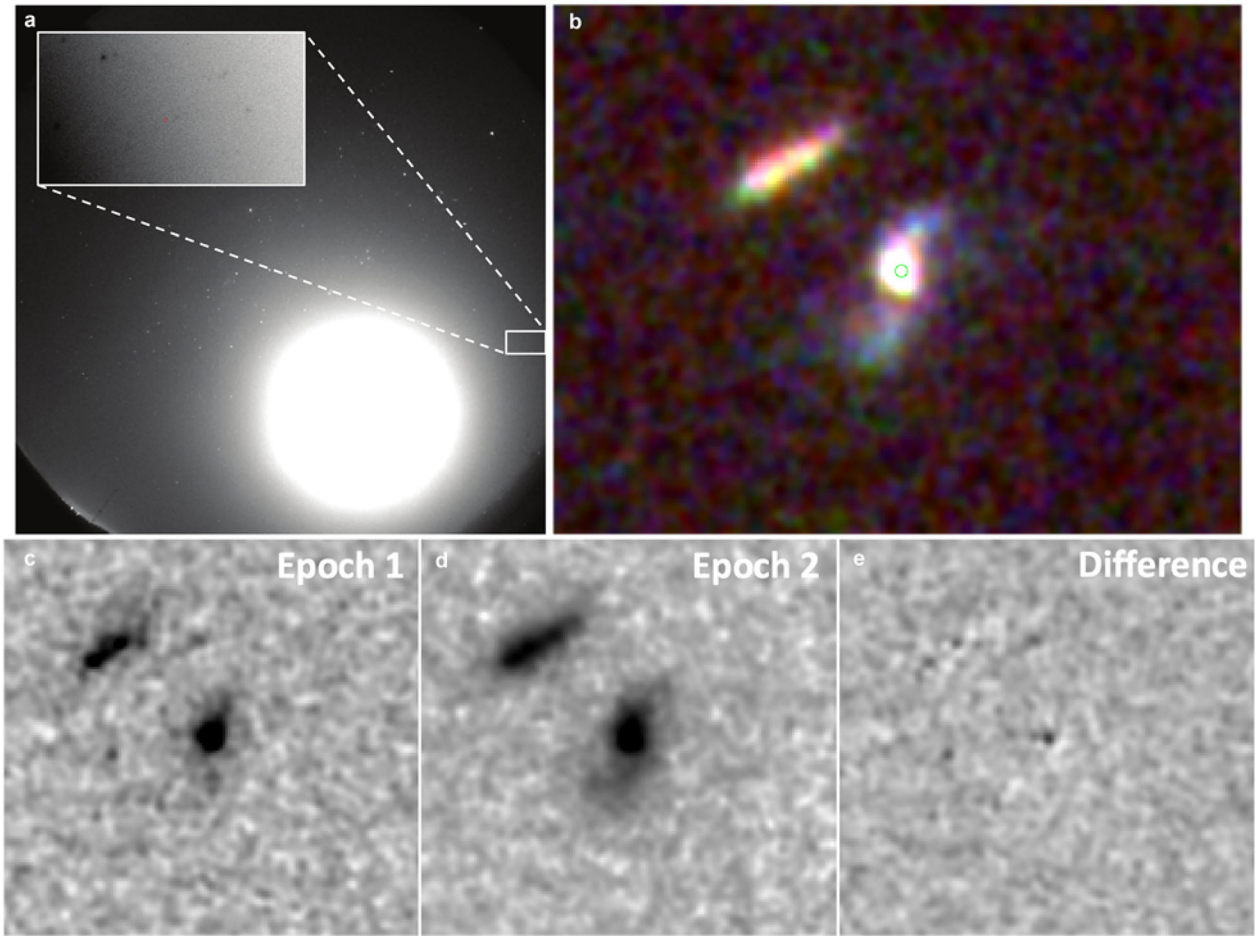

Extended Data Fig. 4 | Images of the localization region of GRB 190114C. **a**, All-sky image captured with the CASANDRA-1 camera at the BOOTES-1 station. The image (30 s exposure, unfiltered) was taken at T_0 + 14.8 s, and was severely affected by the moon. At the GRB190114C location (red dot) no prompt optical emission is detected. Inset, magnification (inverted colours) containing a 10′-diametercircle centred on the optical position. **b**, Three-colour image of the host of GRB 190114C, obtained with the HST. The host galaxy is a spiral galaxy, and the green circle indicates the location of the transient close to its host nucleus. The image is 8″ across; north is up and east is to the left. **c**–**e**, Images of the GRB 190114C field taken with the HST, obtained with the F850LP filter (covering roughly the region from 800 to 1,100 nm). Two epochs, 11 February and 12 March 2019, are shown (images are 4″ across); the right-most image is the result of the difference image. A faint transient is visible close to the nucleus of the galaxy, and we identify this as the late-time afterglow of the burst.

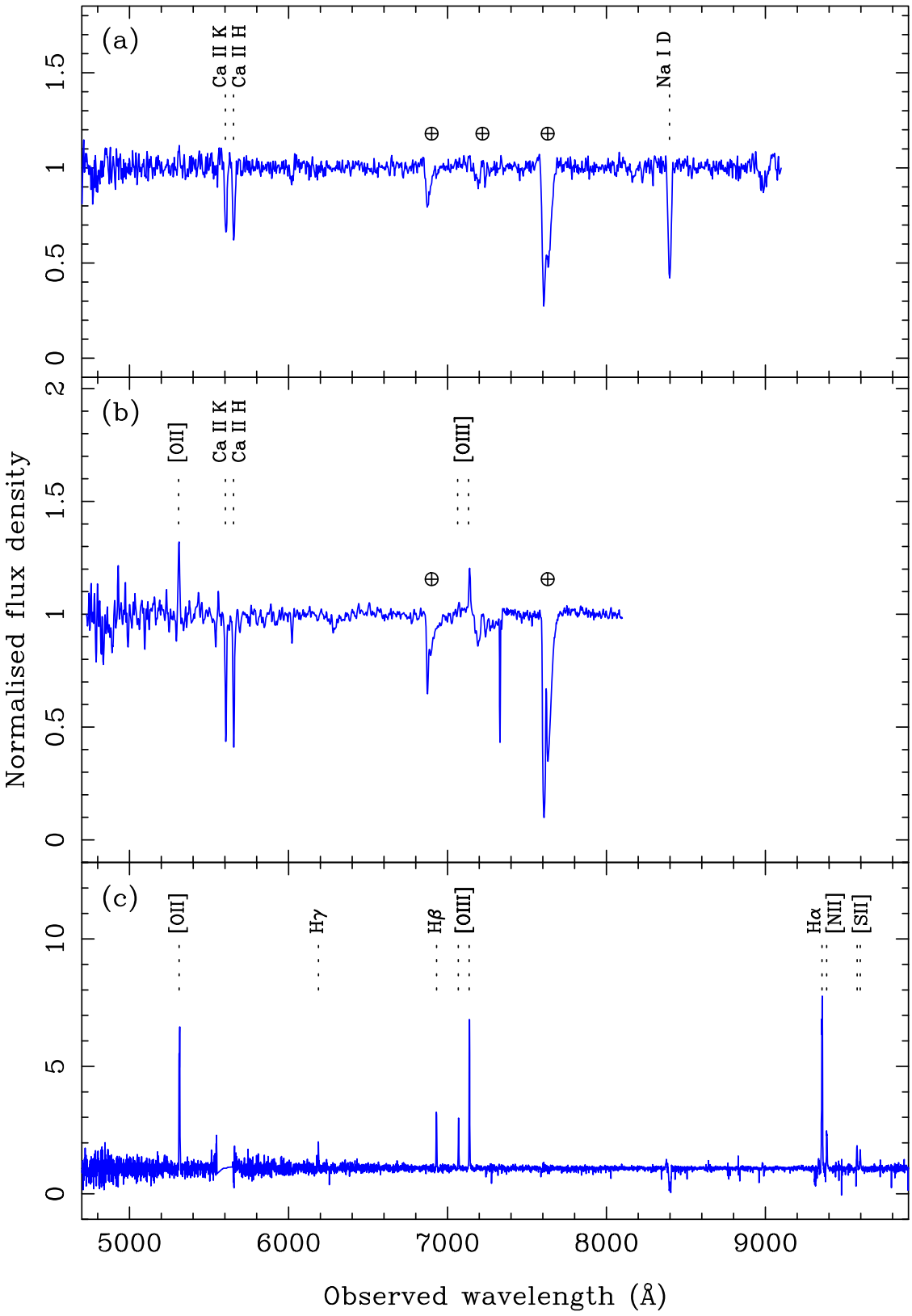

Extended Data Fig. 5 | Optical–NIR spectra of GRB 190114C. a, NOT/AlFOSC spectrum obtained at mid-time (i.e., the epoch corresponding to a half of the exposure length) 1 h post-burst. The continuum is afterglow-dominated at this time, and shows strong absorption features of Ca II and Na I (in addition to telluric absorption). **b**, Normalized GTC (+OSIRIS) spectrum obtained on 14 January 2019, 23:32:03 UT with the R1000B and R2500I grisms. The emission lines of the underlying host galaxy are noticeable, besides the Ca II absorption lines in the afterglow spectrum. **c**, Visible-light region of the VLT–X-shooter spectrum obtained approximately 3.2 d post-burst, showing strong emission lines from the star-forming host galaxy.

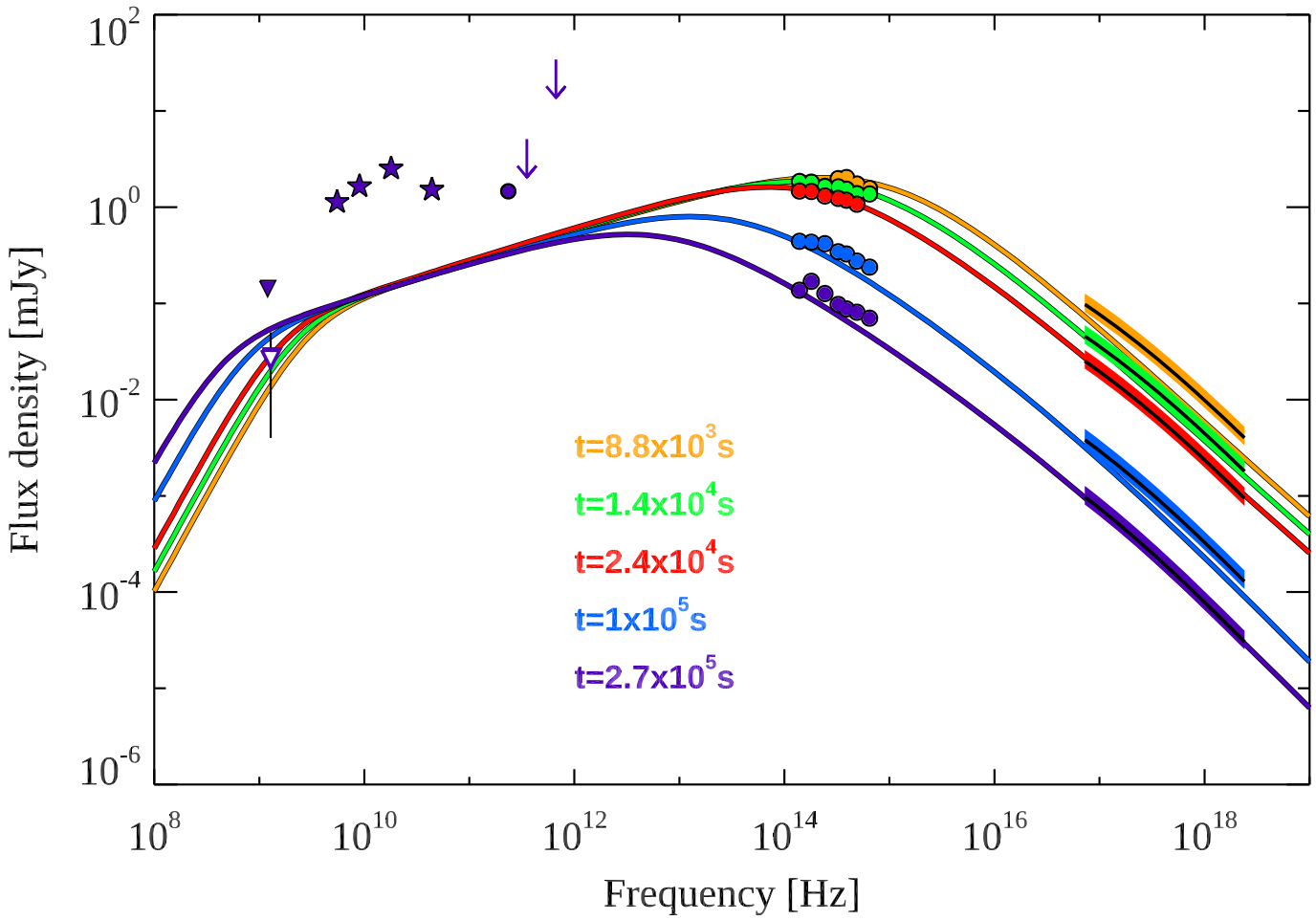

Extended Data Fig. 6 | SEDs from radio frequencies to X-rays at different epochs. The synchrotron frequency ν_m crosses the optical band, moving from higher to lower frequencies. The break between 10^8 and 10^{10} Hz is caused by the self-absorption synchrotron frequency, ν_{sa}. Optical (X-ray) data have been corrected for extinction (absorption). The data points are taken from the following telescopes (from lower to higher frequencies): filled and empty triangle symbols, GMRT and MeerKAT; stars, ATCA; violet filled circle, ALMA, down arrows, JCMT 1σ upper limits; filled circles, LT (yellow) and GROND (all the other colours). Error bars for all data points define the 1σ error. Coloured stripes show the best fit of the XRT data extrapolated to the time of each SED. Their vertical width is obtained from the error (90% confidence level) on the best-fit normalization. Solid lines show the model SEDs for the case $s = 2$.

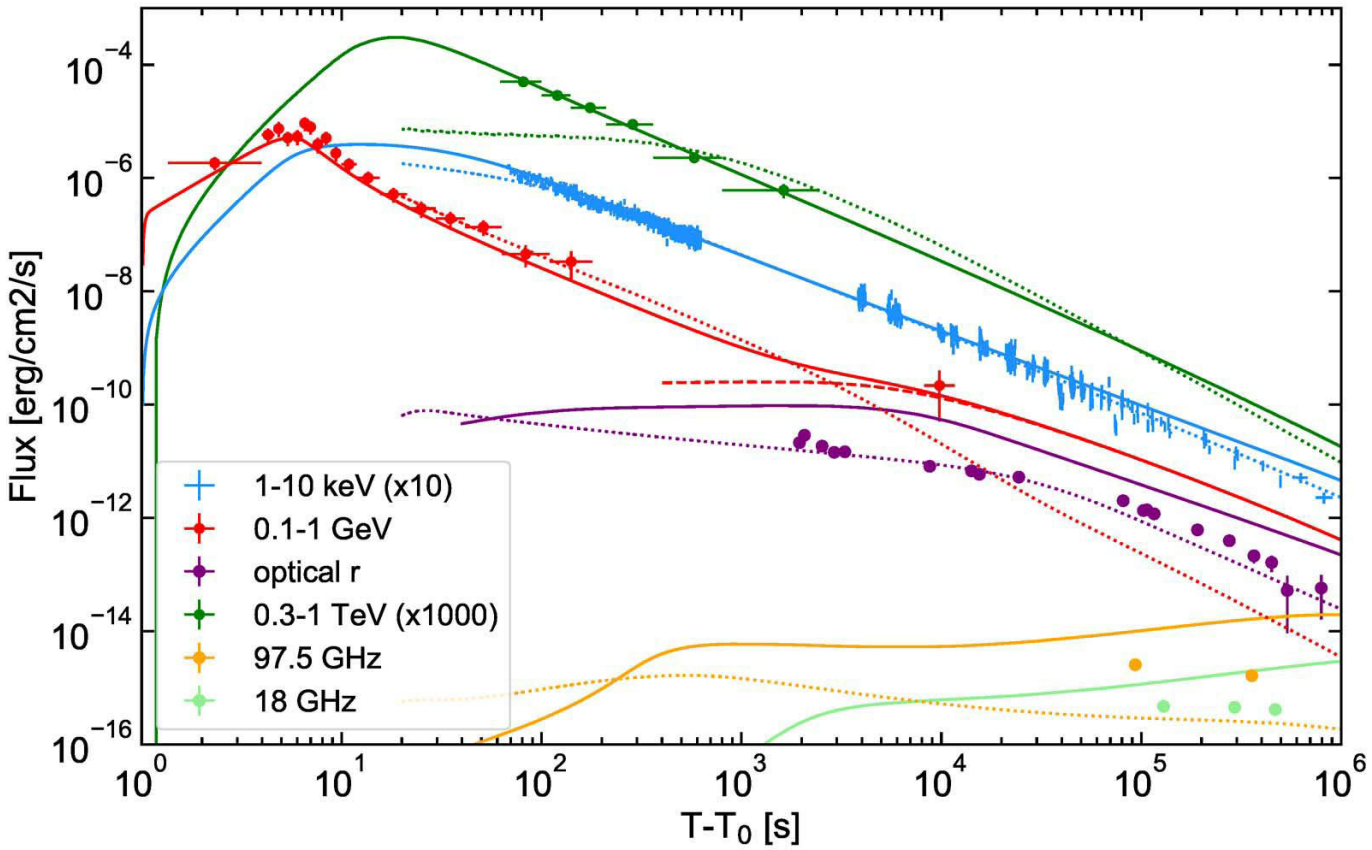

Extended Data Fig. 7 | Modelling of broadband light curves. Modelling results of forward shock emission are compared to observations at different frequencies (see key). The model shown with solid and dashed lines is optimized to describe the high-energy radiation (teraelectronvolt, gigaelectronvolt and X-ray) and has been obtained with the following parameters: $s = 0$, $\varepsilon_e = 0.07$, $\varepsilon_B = 8 \times 10^{-5}$, $p = 2.6$, $n_0 = 0.5$ and $E_k = 8 \times 10^{53}$ erg. Solid lines show the total flux (synchrotron and SSC) and the dashed line refers to the SSC contribution only. Dotted curves correspond to a better modelling of observations at lower frequencies, but fail to explain the behaviour of the teraelectronvolt light curve; they are obtained with the following model parameters: $s = 2$, $\varepsilon_e = 0.6$, $\varepsilon_B = 10^{-4}$, $p = 2.4$, $A. = 0.1$ and $E_k = 4 \times 10^{53}$ erg. Vertical bars on the data points show the 1σ errors on the flux, and horizontal bars represent the duration of the observation.

Extended Data Table 1 | MAGIC spectral-fit parameters for GRB 190114C

Time bin [seconds after T_0]	Normalisation [$\mathrm{TeV^{-1}\,cm^{-2}\,s^{-1}}$]	Photon index	Pivot energy [GeV]
62 – 90	$1.95^{+0.21}_{-0.20} \cdot 10^{-7}$	$-2.17^{+0.34}_{-0.36}$	395.5
68 – 180	$1.10^{+0.09}_{-0.08} \cdot 10^{-7}$	$-2.27^{+0.24}_{-0.25}$	404.7
180 – 625	$2.26^{+0.21}_{-0.20} \cdot 10^{-8}$	$-2.56^{+0.27}_{-0.29}$	395.5
68 – 110	$1.74^{+0.16}_{-0.15} \cdot 10^{-7}$	$-2.16^{+0.29}_{-0.31}$	386.5
110 – 180	$8.59^{+0.95}_{-0.91} \cdot 10^{-8}$	$-2.51^{+0.37}_{-0.41}$	395.5
180 – 360	$3.50^{+0.38}_{-0.36} \cdot 10^{-8}$	$-2.36^{+0.34}_{-0.37}$	395.5
360 – 625	$1.65^{+0.23}_{-0.23} \cdot 10^{-8}$	$-3.16^{+0.48}_{-0.54}$	369.1
625 – 2400	$3.52^{+0.47}_{-0.47} \cdot 10^{-9}$	$-2.80^{+0.48}_{-0.54}$	369.1
62 – 2400 (Nominal MC)	$1.07^{+0.08}_{-0.07} \cdot 10^{-8}$	$-2.51^{+0.20}_{-0.21}$	423.8
62 – 2400 (Light scale +15% MC)	$7.95^{+0.58}_{-0.56} \cdot 10^{-9}$	$-2.91^{+0.23}_{-0.25}$	369.1
62 – 2400 (Light scale -15% MC)	$1.34^{+0.09}_{-0.09} \cdot 10^{-8}$	$-2.07^{+0.18}_{-0.19}$	509.5

For each time bin, the table shows the start and end time of the bin, the normalization factor of the EBL-corrected differential flux at the pivot energy with statistical errors, photon indices with statistical errors, and the pivot energy of the fit (fixed).

Extended Data Table 2 | GROND photometry

T_{GROND}	AB magnitude						
(s)	g'	r'	i'	z'	J	H	K_s
14029.94 ± 335.28	19.21 ± 0.03	18.46 ± 0.03	17.78 ± 0.03	17.33 ± 0.03	16.78 ± 0.05	16.30 ± 0.05	16.03 ± 0.07
24402.00 ± 345.66	19.50 ± 0.04	18.72 ± 0.03	18.05 ± 0.03	17.61 ± 0.03	17.02 ± 0.05	16.53 ± 0.05	16.26 ± 0.08
102697.17 ± 524.01	20.83 ± 0.06	20.00 ± 0.04	19.30 ± 0.04	18.87 ± 0.03	18.15 ± 0.05	17.75 ± 0.06	17.40 ± 0.09
106405.63 ± 519.87	20.86 ± 0.05	19.98 ± 0.03	19.34 ± 0.03	18.88 ± 0.03	18.17 ± 0.06	17.75 ± 0.06	17.34 ± 0.09
191466.77 ± 751.37	21.43 ± 0.07	20.61 ± 0.03	19.97 ± 0.03	19.52 ± 0.03	18.77 ± 0.06	18.28 ± 0.06	17.92 ± 0.14
275594.19 ± 747.59	21.57 ± 0.07	20.88 ± 0.04	20.31 ± 0.04	19.87 ± 0.04	19.14 ± 0.07	18.57 ± 0.06	18.26 ± 0.21
366390.74 ± 1105.79	21.87 ± 0.07	21.17 ± 0.04	20.62 ± 0.03	20.15 ± 0.03	19.43 ± 0.06	18.89 ± 0.06	18.46 ± 0.15
448791.55 ± 1201.33	21.90 ± 0.08	21.27 ± 0.04	20.79 ± 0.04	20.33 ± 0.03	19.66 ± 0.07	18.97 ± 0.07	18.55 ± 0.18
537481.41 ± 1132.16	22.02 ± 0.09	21.52 ± 0.05	21.00 ± 0.04	20.55 ± 0.03	19.87 ± 0.07	19.20 ± 0.07	18.83 ± 0.17
794992.63 ± 1200.69	22.14 ± 0.04	21.51 ± 0.03	21.05 ± 0.04	20.71 ± 0.05	20.31 ± 0.13	19.79 ± 0.14	19.59 ± 0.41
1226716.84 ± 1050.15	22.17 ± 0.04	21.59 ± 0.04	21.26 ± 0.04	20.97 ± 0.04	20.34 ± 0.12	19.95 ± 0.11	19.40 ± 0.34

Time T_{GROND} after the BAT trigger. The AB magnitudes are not corrected for Galactic foreground reddening.

Extended Data Table 3 | LT, NOT and UVOT observations

UTC	Filter	Exposure (s)	Magnitude
		LT/IO:O	
2019-01-14.975	*g*	45	19.08±0.06
2019-01-14.976	*r*	45	18.22±0.02
2019-01-14.977	*i*	45	17.49±0.02
2019-01-14.978	*z*	45	17.12±0.02
2019-01-14.979	*B*	45	19.55±0.15
2019-01-14.980	*V*	45	18.81±0.08
2019-01-15.814	*r*	60	19.61±0.05
2019-01-15.818	*z*	60	18.70±0.06
2019-01-15.820	*i*	60	19.04±0.04
2019-01-15.823	*g*	60	20.96±0.17
		NOT/AIFOSC	
2019-01-14.89127	*g*	1 × 300	17.72±0.03
2019-01-14.89512	*r*	1 × 300	16.93±0.02
2019-01-14.89899	*i*	1 × 300	16.42 ±0.04
2019-01-14.90286	*z*	1 × 300	16.17 ±0.04
2019-01-23.8896	*i*	6 × 300	21.02±0.05

UVOT							
T_{start}	T_{stop}	Filter	Magnitude	T_{start}	T_{stop}	Filter	Magnitude
56.63	57.63	*V*	12.17±0.14	130958	142524	*UVM2*	20.37
57.63	58.63	*V*	12.34±0.14	217406	222752	*UVM2*	20.48
58.63	59.63	*V*	12.44±0.13	107573	125233	*U*	20.29
59.63	60.63	*V*	12.29±0.14	205500	210750	*U*	20.25
60.63	61.63	*V*	12.44±0.14	291188	302718	*U*	20.49
61.63	62.63	*V*	12.16±0.13	400429	412385	*U*	20.82
62.63	63.63	*V*	12.51±0.13	616	627	*V*	16.25±0.20
615.95	625.95	*V*	16.32±0.20	16295	17136	*V*	19.03±0.14
73.34	83.34	*white*	13.86	26775	27682	*V*	19.50±0.27
83.34	93.34	*white*	14.10±0.06	39149	57221	*V*	20.09±0.23
93.34	103.34	*white*	14.19±0.06	108064	125736	*V*	20.02
103.34	113.34	*white*	14.36±0.06	206689	211356	*V*	20.02
113.34	123.34	*white*	14.64±0.06	292383	303996	*V*	20.42
123.34	133.34	*white*	14.65±0.06	401305	413316	*V*	20.17
133.34	143.34	*white*	14.91±0.06	4044	51522	*UVW1*	21.17
143.34	153.34	*white*	14.99±0.06	131216	142656	*UVW1*	20.47
153.34	163.34	*white*	15.05±0.06	217984	223056	*UVW1*	20.57
163.34	173.34	*white*	15.32±0.06	592	612	*UVW2*	17.65
173.34	183.34	*white*	15.38±0.06	6056	56384	*UVW2*	21.30
183.34	193.34	*white*	15.38±0.06	130699	142346	*UVW2*	20.52
193.34	203.34	*white*	15.59±0.06	216828	222404	*UVW2*	20.55
562.0	572.0	*white*	16.96±0.10	566	586	*white*	16.90±0.07
572.0	582.0	*white*	16.90±0.10	607389	613956	*white*	22.16
535.5	555.5	*B*	17.56±0.21	624452	682416	*white*	21.99±0.18
545.5	565.5	*B*	17.25±0.18	745033	769296	*white*	21.64±0.16
285.9	305.9	*U*	17.35±0.19	818840	837216	*white*	22.50
305.9	325.9	*U*	17.50±0.20	893522	907116	*white*	22.57
325.9	345.9	*U*	17.24±0.18	991065	1004196	*white*	22.49±0.35
345.9	365.9	*U*	17.26±0.18	1077542	1094616	*white*	22.41±0.31
365.9	385.9	*U*	17.80±0.24	1140343	1170336	*white*	22.50
385.9	405.9	*U*	17.64±0.22	1220661	1274376	*white*	22.36±0.29
405.9	425.9	*U*	17.82±0.24	5851	6050	*white*	19.25±0.09
425.9	445.9	*U*	17.84±0.25	21950	22857	*white*	20.25±0.09
445.9	465.9	*U*	17.87±0.25	1353459	1359284	*white*	21.70
465.9	485.9	*U*	17.79±0.24	1502211	1548336	*white*	21.98±0.24
485.9	505.9	*U*	17.81±0.24	1692292	1703935	*white*	22.07
505.9	525.9	*U*	17.65±0.22	2132978	2146056	*white*	22.58
542	561	*B*	17.38±0.14	2299521	2317956	*white*	22.41±0.31
5646	5845	*B*	19.54±0.19	63686	80942	*white*	21.07±0.24
21038	46521	*B*	21.14±0.35	107900	125591	*white*	21.40±0.28
62774	96486	*B*	21.33±0.29	206292	211137	*white*	21.52
107737	125412	*B*	21.00	291984	303556	*white*	21.48±0.23
205896	210944	*B*	20.78	401012	413029	*white*	21.84
291586	303137	*B*	21.29	491973	505356	*white*	22.21±0.24
400721	412707	*B*	21.22	74	224	*white*	14.90±0.02
3839	50615	*UVM2*	20.88±0.28				

Magnitudes are SDSS 'AB-like' for ugriz and 'Vega-like' for all the other filters, and they are not corrected for Galactic extinction. For the UVOT data, magnitudes without uncertainties are upper limits.

Extended Data Table 4 | Observations of the host galaxy

Filter	Host	Companion	Combined
Sloan *u*	23.54	25.74	23.40
Sloan *g*	22.51	23.81	22.21
Sloan *r*	22.13	22.81	21.66
Sloan *i*	21.70	22.27	21.19
Sloan *z*	21.51	21.74	20.87
2MASS *J*	20.98	21.08	20.28
2MASS *H*	20.68	20.82	20.00
2MASS *Ks*	20.45	20.61	19.77

For each filter, the estimated magnitudes are given for the host galaxy of GRB 190114C, the companion and the combination of the two objects.

Extended Data Table 5 | Observations of GRB 190114C by ATCA and JCMT SCUBA-2

ATCA			
Start Date and Time	End Date and Time	Frequency GHz	Flux mJy
1/16/2019 6:47:00	1/16/2019 10:53:00	5.5	1.92±0.06
		9	1.78±0.06
		18	2.62±0.26
1/18/2019 1:45:00	1/18/2019 11:18:00	5.5	1.13±0.04
		9	1.65±0.05
		18	2.52±0.27
		44	1.52±0.15
1/20/2019 3:38	1/20/2019 10:25:00	5.5	1.78±0.06
		9	2.26±0.07
		18	2.30±0.23

JCMT SCUBA-2						
UT Date	Time since trigger (days)	Time on source (hours)	Typical 225 GHz CSO Opacity	Typical elevation (degrees)	850 μm RMS density (mJy/beam)	450 μm RMS density (mJy/beam)
2019-01-15	0.338	1.03	0.026	39	1.7	9.2
2019-01-16	1.338	1.03	0.024	39	1.6	8.4
2019-01-18	3.318	0.95	0.031	37	1.7	11.4

For the ATCA data, the start and end dates and times (UTC) of the observations, the frequency and the flux (1σ error) are reported. For the JCMT SCUBA-2 data, the CSO 225-GHz opacity measures the zenith atmospheric attenuation.